www.sciencemag.org/content/359/6382/1411/suppl/DC1

Supplementary Materials for

The biosynthesis of methanobactin

Grace E. Kenney, Laura M. K. Dassama, Maria-Eirini Pandelia, Anthony S. Gizzi,
Ryan J. Martinie, Peng Gao, Caroline J. DeHart, Luis F. Schachner, Owen S. Skinner,
Soo Y. Ro, Xiao Zhu, Monica Sadek, Paul M. Thomas, Steven C. Almo,
J. Martin Bollinger Jr., Carsten Krebs, Neil L. Kelleher, Amy C. Rosenzweig*

*Corresponding author. Email: amyr@northwestern.edu

Published 23 March 2018, *Science* **359**, 1411 (2018)
DOI: 10.1126/science.aap9437

This PDF file includes:

Materials and Methods

Supplementary Text

Figs. S1 to S28

Tables S1 to S3

Captions for Data Files S1 to S7

References

Other supplementary material for this manuscript includes the following:

Data Files S1 to S7 (zipped folder)

Materials and methods

Materials

Unless otherwise specified, chemicals were purchased from MilliporeSigma (Darmstadt, Germany).

Bioinformatic analyses

Genes encoding MbnA, MbnB and MbnC were identified in the NCBI and JGI/IMG databases using the appropriate PFAM or TIGRFAM hidden Markov models (PF05114 for DUF692 proteins and TIGR04159 for MbnBs, although the current version matches only half the *mbnB* gene, TIGR04160 and TIGR04061 for MbnC and related *Pseudomonas* genes, respectively) or via tBLASTn, or via manual annotation for some MbnA sequences (as described previously) (*15*). Phylogenetic tree construction was carried out as previously described (*15*). Sequences were primarily aligned using MAFFT (*42*), and alignments were visualized in Jalview (*43*, *44*). The larger families to which MbnB and MbnC belong were further investigated via protein sequence similarity networks (Files S1-6) constructed with the EFI Enzyme Similarity Tool (EFI-EST) (*45*) using the sequences obtained from the JGI/IMG and the NCBI databases. Sequences with greater than 95% identity were collapsed into a single node, and expectation values were chosen as described previously (*46*) to 45 (DUF692/MbnB) and 25 (MbnC). Metadata were obtained from NCBI or JGI/IMG along with protein sequences, and in some cases manually supplemented. Networks were visualized via Cytoscape 3.1.1 (*47*).

Gene cloning, protein (co-)expression, and protein purification

Initial constructs in the vectors pPR-IBA1 and pPR-IBA2 for separate expression of N- and C-terminally Strep-II-tagged MbnB and MbnC from *Ms. trichosporium* OB3b failed to provide significant amounts of either protein. Instead, Duet vectors (MilliporeSigma, Darmstadt, Germany) were used for co-expression of codon-optimized versions of the two biosynthetic genes. For *Ms. trichosporium* OB3b, vector pACYCDuet-1 was used. In CDS-1, *mbnC* genes were preceded by an N-terminal His_6 tag and a tobacco etch virus (TEV) cleavage site. In CDS-2, a C-terminal Strep-II or S-tag was added to *mbnB* genes. The two coding regions were synthesized as a single piece of DNA and cloned into pACYCDuet-1 via NcoI and XhoI restriction sites (Genscript, Piscataway, NJ). Similarly designed codon-optimized constructs were produced in the Duet vector pCDFDuet-1 for MbnBC pairs from other species, including *Methylosinus* sp. LW3, *Methylocystis hirsuta* CSC1, *Comamonas composti* DSM 21721, *Pseudomonas* sp. ST29, *Gluconacetobacter* sp. SXCC-1, *Vibrio caribbenthicus* BAA-2122, and *Streptomyces katrae* ISP-5550 (Table S2, File S7). Several additional co-expression constructs were tested for *Ms. trichosporium* OB3b, including constructs encoding His_6-MbnB/MbnC-Strep-II, His_6-MbnB/MbnC, and His_6-MbnC/MbnB; metal loading, activity, and oligomeric state were similar to the construct used in this paper (data not shown.) Separately, at the Macromolecular Therapeutics Development Facility (MTDF) at Albert Einstein College of Medicine, twelve MbnA sequences were PCR amplified from gDNA (prepared by G.E.K. using the MasterPure kit as directed (Epicentre, Madison, WI) or purchased from the Deutsche Sammlung von Mikrooganismen und Zellkulturen (DSMZ, Braunschweig, Germany)), and subcloned into pSGC-His and pNYCOMPS vectors. The resulting pSGC-His construct contains 22 additional amino acids and has an N-terminal His_6-tag and a TEV cleavage site. The resulting pNYCOMPS construct contains an additional 18 amino acids and has a C-terminal His_{10}-tag and a TEV cleavage site. Vectors pNYCOMPS and pSGC-His, along with their sequence information, are publicly available at the PSI Materials Repository (http://psimr.asu.edu/)

Mutagenesis of MbnB in *Ms. trichosporium* OB3b MbnBC co-expression constructs was carried out using a QuikChange Lightning kit (Agilent) as directed, except for transformation post-mutagenesis into Top10 cells (Thermo Fisher Scientific, Waltham, MA) to accommodate the chloramphenicol-resistant pACYCDuet-1 plasmid (Tables S2, S3). All MbnB genes were sequenced using the DuetUP2 and T7 terminator primers (ACGT Inc., Germantown, MD)

Plasmids were transformed or co-transformed into the BL21-derived NiCo21(DE3) (New England Biolabs, Ipswitch, MA) or LOBSTR-RIL(DE3) (Kerafast, Boston, MA) strains for protein expression. During the transformation process and the initial switch to liquid medium for an overnight starter culture, LB medium supplemented with appropriate antibiotics was used. For protein expression, instead of LB medium, 6-12 liters of auto-induction medium (*48*) (supplemented with 250-500 μM freshly prepared ferrous ammonium sulfate or ^{57}Fe (Isoflex, San Francisco, CA), anaerobically dissolved under heat in sulfuric acid), were used. Growth was initiated at 37 ºC and 180 rpm in baffled flasks, followed by a cold shift to 18 ºC at 4 h (near the beginning of the auto-induction process). Cells were harvested after overnight growth via centrifugation at 6000 x g for 10 min.

During aerobic purification, cells were resuspended in Buffer A (25 mM MOPS pH 7.2, 250 mM NaCl, 10 mM imidazole, 10% trace metal grade glycerol), thawed in the presence of EDTA-free cOmplete protease inhibitors (Roche Life Sciences, Indianapolis, IN) and DNase (MilliporeSigma, Darmstadt, Germany), and disrupted via sonication on ice for 15 min at 4ºC (1 s:3 s) using a sonic dismembrator (Thermo Fisher Scientific). This lysate was clarified via centrifugation at 125,000 x g for 45 min at 4 ºC, and for His6-tagged proteins and peptides, the supernatant was applied to a Ni-loaded 5 mL HiTrap Chelating Column (GE Healthcare Life Sciences, Chicago, IL). After washing in Buffer A, the protein was eluted via a gradient over 15 column volumes from 0-50% Buffer B (identical to Buffer A, but with 500 mM imidazole), followed by 2 column volumes of 100% Buffer B. Sufficient levels of soluble and stable protein were obtained under these conditions for constructs from all species except *Ms.* sp. LW3 and *St. katrae* ISP-5550. Concentration and buffer exchange into Buffer A was performed using Amicon Ultra-15 concentrators (MilliporeSigma, Darmstadt, Germany) with appropriate molecular weight cutoffs (3 kDa for singly- or co-expressed tagged MbnAs, 10 kDa for MbnB or MbnC produced alone, 30 kDa for co-expressed MbnBC). Aerobic TEV cleavage was not possible for MbnBC due to precipitation in aerobic TEV cleavage buffer. Further aerobic purification was performed using Superdex gel-filtration columns (GE Healthcare Life Sciences, Chicago, IL) pre-equilibrated with Buffer A, including a 120 mL Superdex 75 column for MbnBC, and a 24 mL Superdex Peptide column for tagged MbnAs.

During the anaerobic purification of MbnBC, all steps were performed in an anaerobic glove box (M. Braun, Garching, Germany) maintained at < 0.1 ppm oxygen. MbnBC cell paste was resuspended in lysis buffer (5 mL/g cell paste) containing 50 mM HEPES, pH 7.5, 300 mM KCl, 10% glycerol, 2 mM imidazole, and 10 mM 2-mercaptoethanol. Cells were cooled in an ice bath while being subjected to sixty 10-second pulses from a sonic dismembrator (Thermo Fisher Scientific, Waltham, MA), for a total of 10 min of sonic disruption (80% output). The lysate was then centrifuged at 15,000 x *g* at 4°C. The resulting supernatant was loaded onto a column containing Ni-sepharose excel resin (GE Healthcare Life Sciences, Chicago, IL) equilibrated in lysis buffer. After loading, the column was washed with 20 column volumes of lysis buffer, and eluted with 2 column volumes of elution buffer, composed of lysis buffer with the addition of 500 mM imidazole. Protein-containing fractions were collected and loaded onto a HiPrep 16/60 Sephacryl S-200 size exclusion column (GE Healthcare Life Sciences, Chicago, IL) pre-equilibrated in 50 mM HEPES, pH 7.5, 150 mM KCL, 5% glycerol, and 5 mM DTT. The resulting fractions were pooled and concentrated with an Amicon centrifugal filter unit (10 kDa molecular weight cut-off) (MilliporeSigma, Darmstadt, Germany).

In all cases, protein purity was assessed after the initial purification and after the additional gel-filtration step using SDS-PAGE, either a standard 15% polyacrylamide gel with a standard tris-glycine buffer system (Hoefer, Holliston, MA) or in samples containing tagged or untagged MbnA, a precast 16% or 4-20% Novex tris-tricine gel (Thermo Fisher Scientific, Waltham, MA). Protein concentrations were determined using the calculated extinction coefficient and the absorbance at 280 nm (MbnA) or the Pierce 660 assay (Thermo Fisher Scientific, Waltham, MA) for MbnBC. Visualization of Western blots was performed using an anti-Strep-II HRP conjugate (IBA Lifesciences, Göttingen, Germany), an anti-S-tag HRP conjugate (MilliporeSigma, Darmstadt, Germany) or an anti-His6 HRP conjugate (Thermo Fischer Scientific, Waltham, MA) in combination with a Pierce CN/DAB Susbtrate kit for chromogenic detection (Thermo Fisher Scientific, Waltham, MA.)

Analysis of metal concentration

All inductively coupled plasma optical emission spectroscopy (ICP-OES) and inductively coupled plasma mass spectrometry (ICP-MS) measurements were carried out at the Quantitative Bio-element Imaging Center at Northwestern University. All samples and standards were prepared in 3% trace metal grade nitric acid (MilliporeSigma, Darmstadt, Germany).

ICP-OES experiments were performed on an iCAP 7600 ICP-OES (Thermo Fisher Scientific, Waltham, MA) using multi-element standards (NWU-1, Inorganic Ventures, Christiansburg, VA) containing 0.1-200 ppm As, Cd, Ca, Cr, Co, Cu, Fe, Mg, Mn, Mo, Ni, K, Se, V, and Zn. ICP-MS experiments were performed on an iCap Qc ICP-MS (Thermo Fisher Scientific, Waltham, MA). Samples were prepared as for ICP-OES; standards used the same multi-element solution, but a standard curve was generated using an ESI SC-2DX autosampler/autodilution system, and in-line internal standardization was performed using 1 ng/g of a multi-element solution (IV-ICPMS-71D, Inorganic Ventures, Christiansburg, VA) and the use of KED mode (with H_2 as the collision gas) for accurate quantification of ^{56}Fe and ^{57}Fe. Data analysis was carried out using QTEGRA software v. 2.6 (Thermo Fisher Scientific, Waltham, MA) (Table S1).

Mössbauer spectroscopy

Mössbauer spectra were recorded on constant acceleration Mössbauer spectrometers (SEE Co., Edina, MN) equipped either with a Janis SVT-400 variable-temperature cryostat (weak-field) or a Janis 8TMOSS-OM-12SVT variable-temperature cryostat (strong-field) (Janis, Woburn, MA). All isomer shifts are quoted relative to the centroid of the spectrum of α-iron metal at room temperature. Simulations of Mössbauer spectra were carried out with the program

WMOSS (SEE Co., Edina, MN). Some of the simulations are based on the spin Hamiltonian formalism (see equation below), in which the first term describes the electron Zeeman effect, the second and third terms describe the axial and rhombic zero-field splitting of the total electron spin ground state, the fourth term represents the interaction between the electric field gradient and the nuclear quadrupole moment, the fifth term describes the magnetic hyperfine interactions of the ^{57}Fe nucleus with respect to the total electron spin ground state, and the last term represents the nuclear Zeeman interactions of ^{57}Fe. All symbols have their usual meaning (*49*). Spectra were calculated in the slow relaxation limit.

$$H = \beta S \bullet g \bullet B + \mathrm{D}\left(S_z^2 - \frac{\mathrm{S}(\mathrm{S}+1)}{3}\right) + \mathrm{E}\left(S_x^2 - S_y^2\right) + \sum_i \frac{eQV_{zz,i}}{4}\left[I_{z,i}^2 - \frac{\mathrm{I_i}(\mathrm{I_i}+1)}{3} + \frac{\eta}{3}\left(I_{x,i}^2 - I_{y,i}^2\right)\right] + \sum_i S \bullet A_i \bullet I_i - \sum_i \mathrm{g_n}\beta_n B \bullet I_i$$

Electron paramagnetic resonance spectroscopy

Measurements were performed on an ESP 300 spectrometer (Bruker, Billerica, MA) equipped with an ER 041 MR microwave bridge and an ER 4116DM resonator. Additional methodological details are described in the legend of Fig. S27.

Native mass spectrometry on MbnBC complexes

Samples analyzed by native top down mass spectrometry (nTDMS) were buffer exchanged into 150 mM ammonium acetate with a nominal protein concentration of 10-20 μM. A customized Q Exactive HF mass spectrometer with Extended Mass Range (Thermo Fisher Scientific, Waltham, MA) was utilized for nTDMS analyses (*50*). The nTDMS platform employs direct infusion of sample into a native electrospray ionization (nESI) source held at +2 kV and coupled to a three-tiered tandem MS process. As reported in Belov et al. (*50*) and Skinner et al. (*51*, *52*), the process first includes the analysis of the intact protein complex (MS^1), which provides the total mass (reported as a neutral average mass value). In stage two, the complex is collisionally activated with nitrogen gas to eject monomers (MS^2), thereby liberating the subunits that comprise each intact complex. In stage three, further vibrational activation of the ejected subunits via collisions with neutral gas yields backbone fragmentation products from each monomer (MS^3) that were recorded at isotopic resolution (120,000 resolving power at *m/z* 400). These fragments were used to characterize the primary sequence of the protein and localize post-translational modifications or bound cofactors such as metal atoms.

Intact mass values for MbnBC complexes and ejected subunits were determined by deconvolution to convert data from the *m/z* to the mass domain using mMass (www.mmass.org). Fragmentation data were processed using ProSight Lite (*53*) or ProSightPC 4.0 (Thermo Fisher Scientific, Waltham, MA) to assign recorded fragment ions to the primary sequence of the subunits. Unexplained mass shifts (Δm) observed at the MS^1 and MS^2 levels for the intact complex and subunits, respectively, were manually interrogated using the UNIMOD database as a reference provide candidate modifications. Backbone fragmentation data (MS^3) for MbnB or MbnC with metal ligands were manually annotated using mMass. A detailed illustration of these analyses is provided in Fig. S6.

Standard and stopped-flow UV-vis spectroscopy for MbnA activity assays and MbnA acid hydrolysis assays

Standard UV-visible spectroscopic spectra were collected on an Agilent 8453 spectrophotometer at 10 ºC (temperature controlled via a Peltier unit) (Agilent, Santa Clara, CA), using a quartz cuvette. For simple aerobic activity assays, anaerobic stocks of synthetic MbnA (Bio-Synthesis Inc., Lewisville, TX) in 50% DMF or ACN were thawed in an anaerobic chamber (Coy), and 200 μL of 100 μM protein was prepared in activity buffer (25 mM MOPS pH 7.2, 250 mM NaCl, 10 mM imidazole, 10% molecular biology-grade glycerol). An amount of MbnA sufficient for a final reaction concentration of 125 μM peptide was removed from the anaerobic chamber in a microfuge tube with a screw-on, O-ring cap, and after the peptide was added to the reaction, full spectra were acquired every 15 s. Reactions were stopped via freezing in liquid nitrogen. Acid hydrolysis studies of purified peptide were carried out on the same apparatus, as previously described (*24*).

Stopped-flow absorption spectroscopy experiments were carried out in an anaerobic chamber using an SX20 stopped-flow system (Applied Photophysics, Leatherhead, UK). Reactions included either anaerobically-prepared enzyme and buffer (25 mM MOPS pH 7.2, 250 mM NaCl, 10% glycerol, 10 mM imidazole, O_2-saturated unless otherwise noted) in separate syringes, or anaerobically prepared enzyme in one syringe and substrate peptide mixed with buffer (O_2-saturated unless otherwise noted), prepared for the other syringe immediately prior to loading. All reactions were carried out at 10 ºC and monitored for 300 or 1000 s. Unless otherwise noted, reactions included 100 μM MbnBC, 125 μM MbnA, and ~0.9 mM O_2. Data were processed by using the data analysis and fitting program Kaleidagraph (Synergy Software, Reading, PA).

HPLC purification of modified MbnA

Modified MbnA was purified from reactions of MbnA with MbnBC using reversed-phase C4 columns on an Agilent 1100 series HPLC system equipped with a photodiode array detector (Agilent, Santa Clara, CA). Analytical runs were carried out on a Grace Vydac reverse-phase C4 column (214TP54, 300Å and 5μ, 4.6 mm i.d. x 250 mm) (Grace, Columbia, MD) using a 0-100% gradient of Buffer B (75% ACN, 20% n-PrOH, 1% formic acid) against Buffer A (5% ACN, 1% formic acid) over 30 min at a flow rate of 0.5 mL/min. Semi-preparative runs were carried out using a Grace Vydac column (214TP510, 300 Å and 5 μ, 10 mm i.d. x 250 mm, runtimes adjusted for the increased diameter and a 5 mL/min flow rate) (Grace, Columbia, MD).

Mass spectrometry on MbnA, modified MbnA, Δ*mbnN* Mbn, and acid hydrolysis products

Standard-resolution mass spectrometry experiments were performed on an AmaZonX ion trap mass spectrometer (Bruker, Billerica, MA) using electrospray injection. Samples containing proteins (MbnA/MbnBC reactions) were introduced using a 0-100% gradient of Buffer B (75% ACN, 20% n-PrOH, 1% formic acid) against Buffer A (5% ACN, 1% formic acid) on a Grace Vydac analytical column (214TP54: 300 Å, 5 μ, 4.6 mm i.d. x 250 mm, gradient for 30 min at 1 mL/min) or LC-MS column (214TP5405: 300 Å, 5 μ, 4.6 mm i.d. x 50 mm, runtimes adjusted for a 0.5 mL/min flowrate and the shorter column length) (Grace, Columbia, MD).

High-resolution mass spectrometry and tandem mass spectrometry experiments

If necessary, samples were prepared by incubating with 2.5 mM dithiothreitol in 50 mM ammonium bicarbonate pH 7.8 solution at 37 ºC for 1 h to reduce disulfides in MbnA. Samples were then analyzed by high-resolution, tandem mass spectrometry (MS/MS) using a Thermo Q-Exactive (Thermo Fisher Scientific, Waltham, MA) in line with an electrospray source and an Agilent 1200 series HPLC stack including a binary pump, degasser, and autosampler (Agilent, Santa Clara, CA), outfitted with a column (Grace Vydac 214tp54 C4 250 x 4.6 mm 5 μ particle size with matching guard) (Grace, Columbia, MD). Mobile phase A was 5% acetonitrile:1% formic acid:94% water; B was 75% acetonitrile:20% *n*-propanol:1% formic acid:4% water. The gradient was as follows: at 0 min, 100% A; 60 min, 100% B; with a flow rate of 500 μL/min. A 1:4 split was used to transfer 20% of the eluting sample from the column to the electrospray source, decreasing the flow rate into the electrospray ionization source to 100 μL/min. The capillary of the ESI source was set to 275 °C, with sheath gas at 10 arbitrary units, the auxiliary gas at 5 arbitrary units and the spray voltage at 4.0 kV. In positive polarity mode, MS^1 data was collected at a resolving power of 70,000 (at *m/z* 200). The precursor ion was subsequently fragmented using higher energy collisional dissociation (HCD) set to 22% normalized collision energy in MS^2 at a resolving power of 35,000. Data analysis was performed using QualBrowser and visualized using ProSight Lite (*53*).

Methanotroph growth conditions

Ms. trichosporium OB3b cells (both wild-type and mutant strains) were grown as previously described (*54*). Cells and spent medium were harvested at late-exponential phase growth. Small-scale 50 mL cultures were grown at 30 ºC and 200 rpm in 250 mL flasks, sealed with rubber septa and under a 1:3 methane:air ratio. Medium-scale cultures were grown in 1 L spinner flasks (Chemglass Life Sciences, Vineland, NJ) or a 2.5 L bioreactor (Chemglass Life Sciences, Vineland, NJ) at 30 ºC with stirring at 200 and 300 rpm, respectively, and constant sparging with a gas mix containing a 1:3 ratio of methane to air. Large-scale cultures were grown as previously described in a BioFlo 510 fermenter (Eppendorf, Hamburg, Germany) (*24*). Gentamicin (2.5 μg/mL) was added only to small-scale growths of cultures containing mutant strains.

Ms. trichosporium OB3b *mbnN* knockout construction

The *Ms. trichosporium* OB3b *ΔmbnN* mutant was generated by chromosomal gene disruption using methods previously described (*55*). The middle of the *mbnN* encoding gene was disrupted by introduction of a gentamicin resistance gene through homologous recombination (Fig. S28). DNA regions 550 bps upstream and downstream of the middle of the *mbnN* gene were amplified to flank a gentamicin resistance gene (Table S3). The PCR products were assembled into the mobilization vector pK18mobsacB using Gibson assembly and transformed into *E. coli* S17-1 ATCC 47055 (American Type Culture Collection, Manassas, VA) to produce plasmid pSYR13. This gene disrupting plasmid was introduced into *Ms. trichosporium* OB3b through conjugation. *E. coli* S17-1 and *Ms. trichosporium* OB3b cells were plated together onto NMS mating plates supplemented with LB. After two days, the cells were plated onto NMS selection plates containing kanamycin (25 μg/mL) and nalidixic acid (10 μg/mL). Transconjugants were plated onto NMS plates containing gentamicin (10 μg/mL) and 2.5% sucrose for counter selection to ensure double homologous recombination. Colonies were screened by PCR for the correct mutant genotype and were grown at 30 °C in 50 mL NMS medium with gentamicin (5 μg/mL), no copper, and a gas mix containing a 1:3 methane-to-air ratio.

Mbn isolation, purification, and characterization

Mbn-producing wild-type and mutant Δ*mbnN* *Ms. trichosporium* OB3b cells were grown in a 12 L fermenter (Eppendorf, Hamburg, Germany) in medium containing 0.1 μM $CuSO_4$ as described previously (*24*). Clarification of spent medium, initial purification on a Diaion HP-20 column (MilliporeSigma, Darmstadt, Germany), and further purification on preparative reverse-phase C18 columns were performed as described previously (*24*). UV-visible spectroscopic analysis, acid hydrolysis, and ESI-LC-MS experiments were also carried out as described previously (*24*).

Supplemental Text

Comments on the Mössbauer and EPR spectra of MbnBC complexes

We have studied MbnBC complexes from three different organisms, *Ms. trichosporium* OB3b, *Co. composti* DSM 21721, and *Ps.* sp. ST29, by a combination of Mössbauer and EPR spectroscopies. In general, samples of MbnBC complexes from these three organisms are heterogeneous and contain multiple species. The analysis presented below suggests that the two principal components are an antiferromagnetically coupled dinuclear $[Fe(III)]_2$ cluster with an $S_{tot} = 0$ ground state (~35% of total Fe) and an exchange-coupled trinuclear $[Fe(III)]_3$ cluster with an $S_{tot} = 5/2$ ground state (~55% of total Fe). However, the complexity of the spectral features and heterogeneity of the samples have thus far precluded a detailed characterization of the trinuclear cluster. Of the three MbnBC complexes, we have studied *Ms. trichosporium* OB3b MbnBC in greatest detail.

The 160 K/zero-field Mössbauer spectrum of aerobically isolated *Ms. trichosporium* OB3b MbnBC (Fig. S5A, vertical bars) displays a broad quadrupole doublet with parameters (isomer shift (δ) of 0.47 mm/s and quadrupole splitting parameter (ΔE_Q) of 0.85 mm/s), Fig. S5A, black line) that are typical of high-spin Fe(III) (*49*). These parameters are also consistent with a low-spin Fe(II) configuration, but we disfavor this assignment because the proposed Fe ligands (side chains of MbnBC-derived Glu/Asp and His residues and solvent-derived water and/or hydroxide) are weak-field ligands; strong-field ligands capable of stabilizing low-spin Fe(II) configuration, like carbon monoxide and cyanide, are observed in only a few biological systems, such as hydrogenases (*56*). The weak absorption at ~2.8 mm/s (indicated by an arrow) is at a position typical for the high-energy line of high-spin Fe(II) and reveals that the sample contains less than ~5% of high-spin Fe(II).

The 4.2 K/53 mT spectrum of that sample (Fig. S5B, vertical bars) displays a lesser amount of the quadrupole doublet, while the remainder of the spectrum displays broad, paramagnetically split features that emanate from one (or more) Fe species. The observation of a quadrupole doublet with parameters of high-spin Fe(III) suggests the presence of an antiferromagnetically coupled $[Fe(III)]_2$ cluster with $S_{tot} = 0$ ground state. This assumption is confirmed in spectra collected in externally applied fields (see below). Further support for a dinuclear cluster is obtained by EPR spectroscopy, which reveals a weak signal for a complex with $S_{tot} = 1/2$ with $g_{av} < 2$, as expected for an antiferromagnetically coupled high-spin [Fe(II)/Fe(III)] complex (Fig.

S27A). Identical Mössbauer-spectroscopic features would be expected for clusters of higher nuclearity containing an *even* number of high-spin Fe(III) centers. For example, tetranuclear clusters with $[\mathrm{Fe(III)}_4(\mu_3\text{-O})_2]^{8+}$ and $[\mathrm{Fe(III)}_4(\mu_2\text{-O})_2(\mu_2\text{-OH})_4]^{4+}$ core structures exhibit $S_{\mathrm{tot}} = 0$ ground states (*57-59*). However, a tetranuclear $\mathrm{Fe(III)}_4$ cluster is inconsistent with other data on MbnBC complexes, and so we disfavor this possibility.

The broad magnetically split features are typically observed for complexes with a half-integer electron spin ground state (*49*, *60*). The presence of one (or more) species with $S_{\mathrm{tot}} = 5/2$ ground state is supported by the EPR spectrum, which displays the hallmark signal at $g_{\mathrm{eff}} = 4.3$ that is indicative of a complex with $S_{\mathrm{tot}} = 5/2$ in the rhombic limit ($E/D \sim 1/3$; Fig. S27B). The broadness and lack of resolution of the magnetically split features in the 4.2 K/53 mT Mössbauer spectrum suggests that the fluctuation rate of the electron spin of the corresponding Fe species is comparable to the time scale of the Mössbauer experiment (*viz* the spectrum is in the so-called intermediate relaxation regime). Indeed, the 2 K/53 mT spectrum of this sample (Fig. S5C, vertical bars) is markedly different and displays sharper and better resolved magnetically split features. The spectrum is almost completely independent of the orientation of the externally applied magnetic field relative to the propagation direction of the γ beam (see solid line in Fig. S5C for 2 K/53 mT spectrum collected with external field oriented perpendicular to the γ beam), consistent with the highly anisotropic spin expectation value, $\langle \mathbf{S} \rangle$, of the ground Kramers doublet of a $S_{\mathrm{tot}} = 5/2$ system with $E/D \sim 1/3$.

Further insight into the electronic structure of the two main components is obtained from Mössbauer spectra collected in strong externally applied magnetic fields oriented parallel to the γ-beam. Importantly, the features of the paramagnetic complex(es) are reasonably well resolved in these spectra and allow us to draw some important conclusions. Comparison of the outermost features of the variable-field spectra (Fig. S5D) reveals that the separation of some of the outer lines decreases with increasing external field (solid arrows in Fig. S5D). This behavior is typical for Fe sites with a half-integer electron spin ground state. Conversely, for some lines, separation increases with an increasing external field (dashed arrows in Fig. S5D). This behavior is typically observed for an Fe site of an exchange-coupled cluster with a half-integer spin ground state, for which the local spin of Fe site is oriented antiparallel to the total spin, i.e. for Fe sites that have a negative spin projection factor (*49*, *60*). Increased splitting of the spectra with increasing external field can also be observed for paramagnetic Fe complexes with an integer-spin ground state. We disfavor this possibility both because such complexes would require an even number of high-spin Fe(III) sites and those high-spin Fe(III) complexes have generally a $S_{\mathrm{tot}} = 0$ ground state, and because the experimentally observed increase of the splitting would require a linear increase of the spin expectation value with increasing field. The parameters required to simulate this behavior are not physically meaningful.

The position of the lines as a function of the external field is consistent with the presence of an exchange-coupled trinuclear cluster with three spectroscopically distinct high-spin Fe(III) sites, of which the local spins of two sites, $\mathrm{Fe_A}$ and $\mathrm{Fe_B}$, are oriented parallel to the total electron spin ground state, while the local spin of the remaining site, $\mathrm{Fe_C}$, is oriented antiparallel to the total electron spin ground state. Because the EPR spectrum of an identical sample indicates the presence of a complex with a near-rhombic $S_{\mathrm{tot}} = 5/2$ ground state, we have analyzed the high-field spectra using the commonly used spin Hamiltonian formalism in the frame of the $S_{\mathrm{tot}} = 5/2$

total electron spin ground state with three high-spin Fe(III) subsites. To minimize the number of parameters, we allowed the values of δ and ΔE_Q to deviate less than 0.05 mm/s compared to the values of the 160 K/zero-field spectrum. Furthermore, we initially kept the three Fe(III) hyperfine tensors, $\mathbf{A}_{Fe}$, isotropic, because high-spin Fe(III) sites typically exhibit generally isotropic $\mathbf{A}_{Fe}$ tensors. In order to match the shape and position of the lines better, we have then allowed the three principal components of all three $\mathbf{A}_{Fe}$ tensors to vary slightly (within ~5%). In addition, the portion of the spectrum associated with the putative $[Fe(III)]_2$ cluster can be simulated with the parameters of the quadrupole doublet subspectrum of the 2 K/53 mT spectrum (δ = 0.48 mm/s and ΔE_Q = 0.85 mm/s) and assuming a diamagnetic ($S_{tot} = 0$) ground state. The combined simulations are depicted as solid blue lines in Figs. S5E-H, while those of the individual Fe sites are shown color coded (Figs. S5E-H, red, orange, and green lines for the three Fe sites of the $[Fe(III)]_3$ cluster and black lines for the two indistinguishable Fe sites of the $[Fe(III)]_2$ cluster using parameters given in the legend of Fig. S5.

Importantly, because the local (intrinsic) $\mathbf{a}_{Fe}$ tensors of high-spin Fe(III) sites have values of ~-20T to ~-22T (*49*), the observed $\mathbf{A}_{Fe}$ tensors with respect to the total electron spin ground state allow the spin projection factors, c_i i=1-3, of the three sites to be investigated. Their values are ~+0.96, ~+0.87, and ~-0.64. These values are similar to those expected for a trinuclear $[Fe(III)]_3$ cluster, in which one Fe(III) site (Fe_C) is antiferromagnetically coupled to the other two Fe(III) sites (Fe_A and Fe_B), while the exchange coupling between Fe_A and Fe_B is smaller. For $J_{AC} = J_{BC}$ [$= J$] and $J_{AB}/J < 0.5$ such a spin system exhibits a ground state with $S_{tot} = 5/2$, $S_{AB} = 5$ and spin projection coefficients $c_A = c_B = +6/7$ (0.86) and $c_C = -5/7$ (-0.71) (*61*). These values are in reasonably good agreement with the experimentally determined values, when considering the simplicity of the model. The experimentally observed difference of c_A and c_B can be rationalized by the fact that J_{AC} and J_{BC} are likely not identical, leading to different values of c_A and c_B. Importantly, the putative spatial arrangement of the trinuclear cluster of MbnBC (Fig. S21) is consistent with the electronic structure deduced by Mössbauer and EPR spectroscopies.

In addition to these two components, there is a minor amount (~15% of total Fe) of one or more not-yet identified paramagnetic Fe(III) complex(es). The fact that the remaining features are also associated with high-spin Fe(III), exhibit a paramagnetic ground state, but with a diminished splitting (compared to the $[Fe(III)]_3$ complex with $S_{tot} = 5/2$), might suggest that these have a $S_{tot} = 1/2$ and/or $S_{tot} = 3/2$ ground state. For $0.5 < J_{AB}/J < 0.8$, the ground state has $S_{tot} = 3/2$ and $S_{AB} = 4$ and for $0.8 < J_{AB}/J < 1$, the ground state has $S_{tot} = 1/2$ and $S_{AB} = 3$.

Mössbauer spectra of aerobically isolated *Co. composti* DSM 21721 MbnBC (Figs. S5I-M, blue solid lines) and *Ps.* sp. ST29 MbnBC (Figs. S5N, O) are similar to those of aerobically isolated *Ms. trichosporium* OB3b MbnBC and also exhibit the above described features associated with the diamagnetic ($S_{tot} = 0$) $[Fe(III)]_2$, paramagnetic ($S_{tot} = 5/2$) $[Fe(III)]_3$, and unidentified paramagnetic Fe(III) complex(es), although in slightly different relative amounts (19 and 36% diamagnetic $[Fe(III)]_2$ cluster, ~55 and ~52% paramagnetic $S_{tot} = 5/2$ $[Fe(III)]_3$ cluster, and ~26 and ~12% not-yet identified Fe(III) complex(es) in *Co. composti* DSM 21721 and *Ps.* sp. ST29 MbnBC, respectively (spectra of *Ms. trichosporium* OB3b MbnBC recorded under identical conditions are shown in Figs. S5I-O and are depicted with solid lines for comparison). We note that the quantification of species for *Ps.* sp. ST29 MbnBC is less certain than quantification of species present in *Ms. trichosporium* OB3b and *Co. composti* DSM 21721 since fewer field-dependent spectra were collected.

In addition, we have studied a sample of anaerobically isolated *Ps.* sp. ST29 MbnBC (Fig. S5P, Q, vertical bars). Comparison of the spectra of anaerobically isolated to those of aerobically isolated *Ps.* sp. ST29 MbnBC suggests the presence of a similar amount of the paramagnetic species, but a lesser amount of the $[Fe(III)]_2$ cluster with $S_{tot} = 0$ in the spectrum of anaerobically isolated *Ps.* sp. ST29 MbnBC. Conversely, the spectrum of anaerobically isolated *Ps.* sp. ST29 MbnBC contains a larger amount of high-spin Fe(II) (or $[Fe(II)]_2$) species.

Ongoing studies aim at a more detailed characterization of the various Fe-containing species in MbnBC complexes from various sources and the identification of the active form.

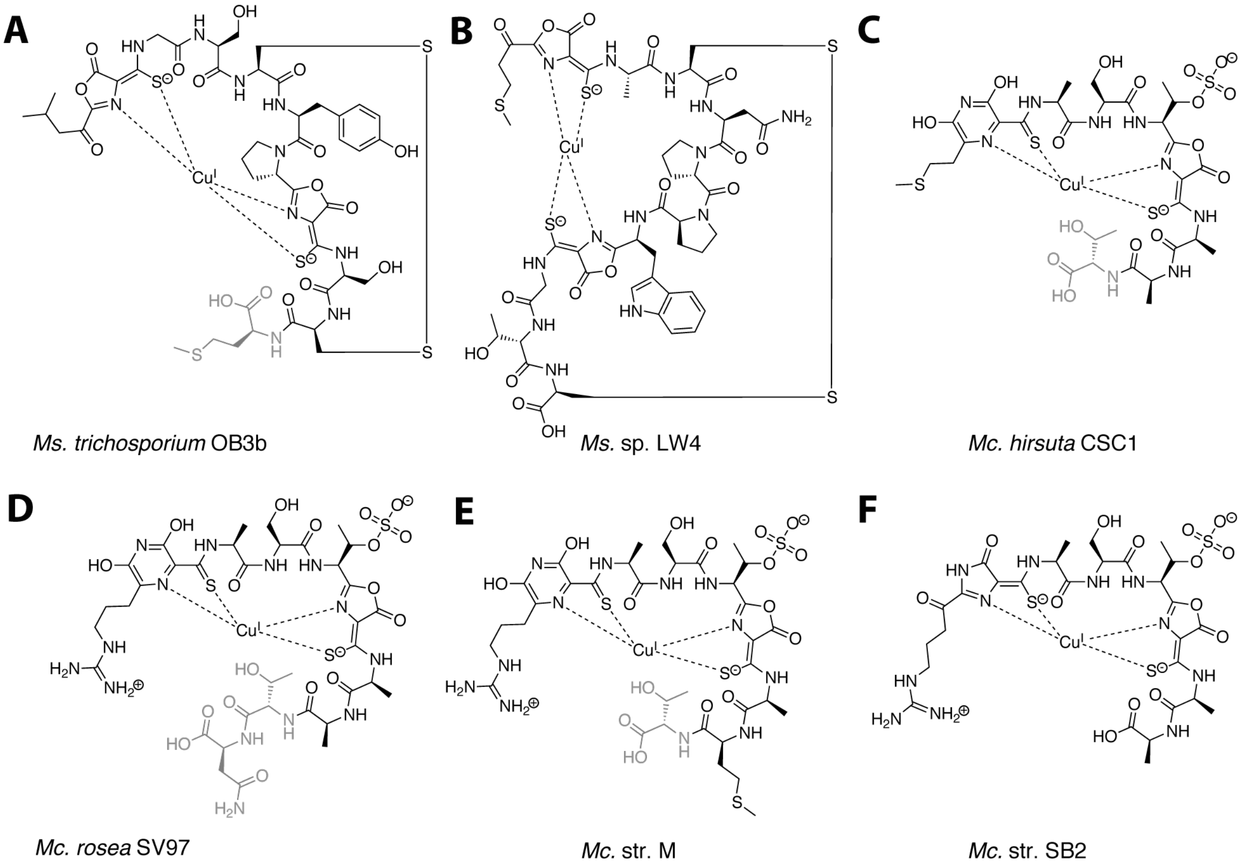

Ms. trichosporium OB3b

Ms. sp. LW4

Mc. hirsuta CSC1

Mc. rosea SV97

Mc. str. M

Mc. str. SB2

Fig. S1. Structures of characterized Mbns.

Residues shown in gray are sometimes absent in significant portions of the natural product as recovered from the spent medium. Based on the sequences of the precursor peptides, there are likely additional residues lost for all *Mc.* Mbns (the five residues following the second oxazolone/thioamide are AATNG for all *Mc.* species except *Mc.* sp. M, where they are AMTNG). (**A**) *Ms. trichosporium* OB3b CuMbn contains two oxazolone-thioamide moieties. (**B**) *Ms.* sp. LW4 CuMbn contains two oxazolone-thioamide moieties. (**C**) *Mc. hirsuta* CSC1 CuMbn contains two heterocycle-thioamide moieties, but the first heterocycle is a pyrazinediol (or a (hydroxy)pyrazin(edi)one tautomer), as identified via mass spectrometry and X-ray crystallography. (**D**) *Mc. rosea* SV97 CuMbn and (**E**) *Mc.* sp. M CuMbn similarly have a pyrazinediol (or a (hydroxy)pyrazin(edi)one tautomer) in the first heterocycle-thioamide position. (**F**) *Mc.* sp. SB2 CuMbn additionally has a non-oxazolone heterocycle in the first position. Although it has been described as an imidazolone on the basis of NMR data, the absence of a crystal structure and the exceedingly high identity between the *Mc. rosea* SV97 and *Mc.* str. SB2 operons raises the question of whether the heterocycle in both species is in fact a (hydroxy)pyrazin(edi)one tautomer.

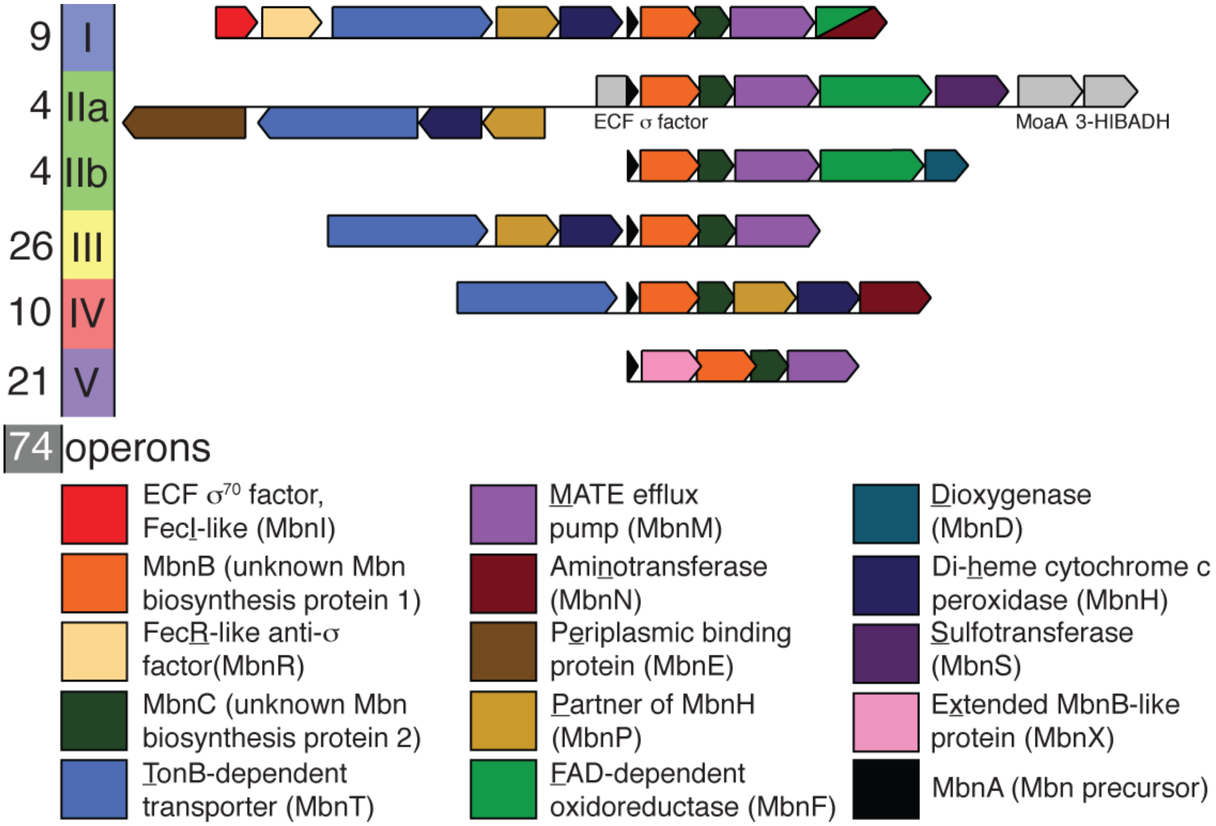

Fig. S2. Mbn operons by group.

The total number of operons in each group is listed to the left of the operon, and a color-coded list of genes is shown below the operons. Representatives of the various operon families discussed in this paper include *Ms. trichosporium* OB3b (I), *Mc. hirsuta* CSC1 (IIa), *Mc.* sp. LW3 (IIb), *Co. composti* DSM21721 (III), *Ps.* sp. ST29 (III), *Gl.* Sp. SXCC-1 (IV), *Vi. caribbenthicus* BAA-2122 (V), and *St. katrae* ISP-5550 (V).

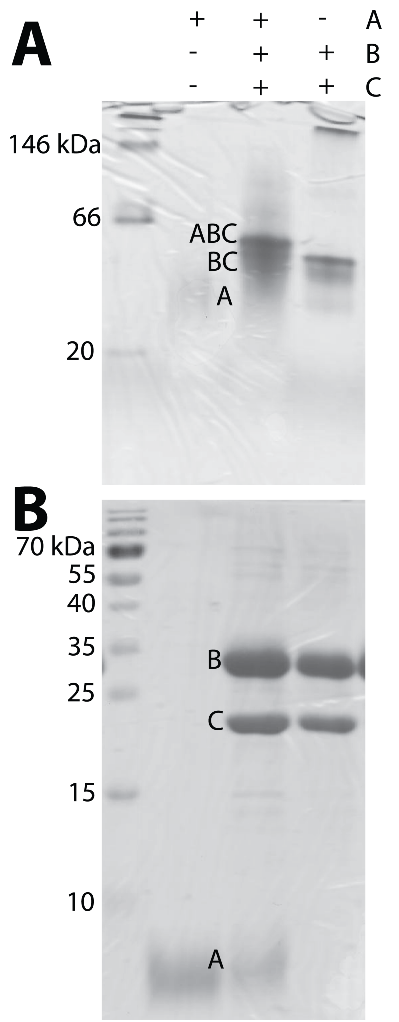

Fig. S3. Polyacrylamide gel electrophoresis supports the formation of a heterodimeric MbnBC and a 1:1:1 MbnABC complex.

(**A**) Blue native-PAGE and (**B**) denaturing SDS-PAGE for Mbn(A)BC from *Ms. trichosporium* OB3b.

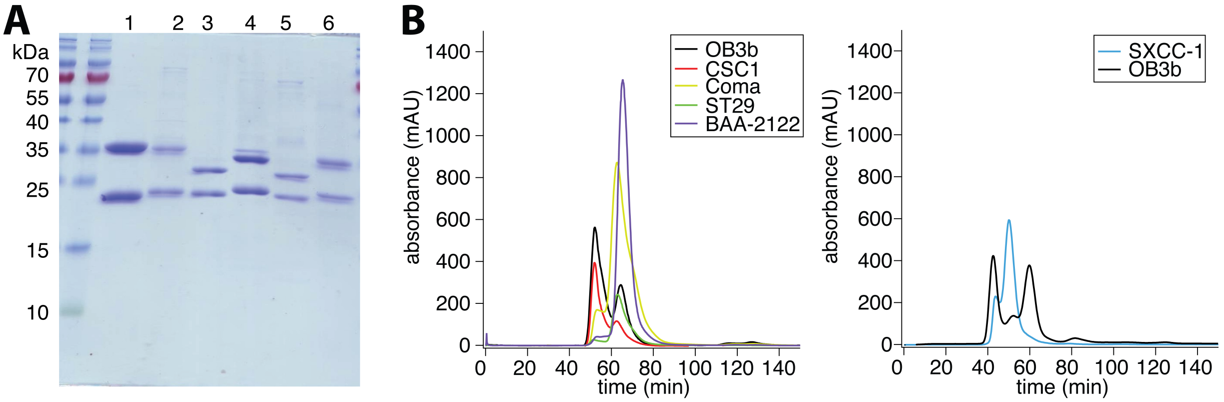

Fig. S4. MbnBC constructs (consisting of His$_6$-MbnC and either MbnB-strep or MbnB-S•tag) for a range of species containing Mbn operons.

(**A**) Denaturing SDS-PAGE gel for constructs from 1) *Ms. trichosporium* OB3b (Group I), 2) *Mc. hirsuta* CSC1 (Group IIa), 3) *Co. composti* DSM 27171 (Group III), 4) *Ps.* Sp. ST29 (Group III), 5) *Gl.* Sp. SXCC-1 (Group IV), and 6) *Vi. caribbenthicus* BAA-2122 (Group V). (**B**) Chromatograms for the preparative purification of all constructs on a Superdex 75 gel filtration column. After the elution of higher order oligomers in the void volume (the first peak observed in all chromatograms), all constructs eluted as a heterodimer except for the *Gl.* sp. SXCC-1 construct, which was purified on Superdex 75 column with a decreased bed volume (shown to the right along with the *Ms. trichosporium* OB3b construct for comparison); the earlier elution point is potentially consistent with a dimer of dimers, though it is not clear whether this is physiologically relevant. Masses for each complex were confirmed by nTDMS.

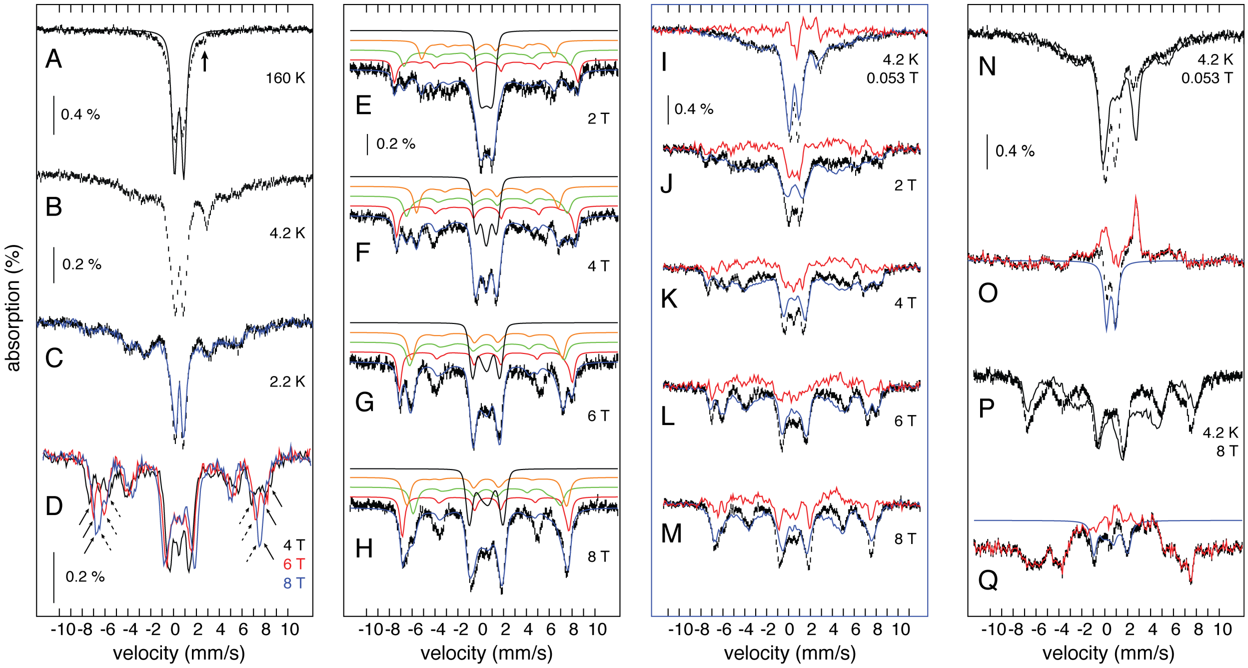

Fig. S5. Field-dependent Mössbauer spectra of the MbnBC complex.

Mössbauer spectra (black vertical bars) of aerobically-isolated *Ms. trichosporium* OB3b MbnBC, collected at 160 (**A**), 4.2 (**B**) and 2.2 (**C**) K in the presence of a 53 mT applied magnetic field oriented parallel to the propagation of the γ beam. A spectrum collected at 2.2 K with the field applied perpendicular to the γ beam is overlaid (**C**, blue solid line). (**D**) Spectra of *Ms. trichosporium* OB3b MbnBC, collected in the presence of varying applied magnetic fields (4, 6, and 8 T; black, red, and blue solid lines, respectively) at 4.2 K. Lines that move outward with increasing applied magnetic field are highlighted by dashed arrows, whereas those moving inward are highlighted by solid arrows. (**E-H**) Field-dependent Mössbauer spectra (black vertical bars) of *Ms. trichosporium* OB3b MbnBC collected with applied magnetic fields of 2.0 T (**E**), 4.0 T (**F**), 6.0 T (**G**), and 8.0 T (**H**). A four-component simulation is overlaid (blue solid lines), comprising a diamagnetic component (black solid line) and three additional components (red, green, and orange solid lines) consistent with three unique sites in a triferric cluster with overall spin $S_{\text{tot}} = 5/2$. The diferric cluster was simulated with δ = 0.49 mm/s, ΔEq = 0.80 mm/s, and η = 0.8, comprising 32% of total iron. The triferric cluster was simulated with three components having δ = 0.52, 0.44, and 0.55 mm/s, respectively; ΔEq = 0.80, 0.90, 0.80 mm/s, respectively; η = -0.8, -1.8, and -2.1, respectively; and hyperfine tensors [-21.9, -21.3, -20.0], [-18.0, -19.4, -18.0], and [+14.7, +14.1, +16.0] T, respectively, comprising 59% of the total iron. (**I-M**) Overlay of the Mössbauer spectra of *Ms. trichosporium* OB3b (black vertical bars) and *Co. composti* DSM 21721 (blue solid line) MbnBC collected with varying applied magnetic fields; difference spectra obtained by subtracting the *Co. composti* DSM 21721 MbnBC spectrum from the *Ms. trichosporium* OB3b MbnBC spectrum at each applied magnetic field (red solid line). (**N-Q**) Comparison of aerobically- and anaerobically-isolated *Ps.* sp. ST29 MbnBC Mössbauer spectra, collected at 4.2 K in the presence of 0.053 T (**N**) and 8 T (**P**) applied magnetic field. Aerobically-isolated spectra (black vertical bars) are overlaid with anaerobically-isolated spectra (black solid lines). Difference spectra (**O** and **Q**, black vertical bars) were obtained by subtracting the spectrum of the anaerobically-isolated sample from the spectrum of the aerobically-isolated sample (100% intensity). Diamagnetic spin Hamiltonian simulations are overlaid (blue solid lines, 20% intensity); the difference spectra obtained by subtracting the simulations from the experimental spectra are also overlaid (red solid lines).

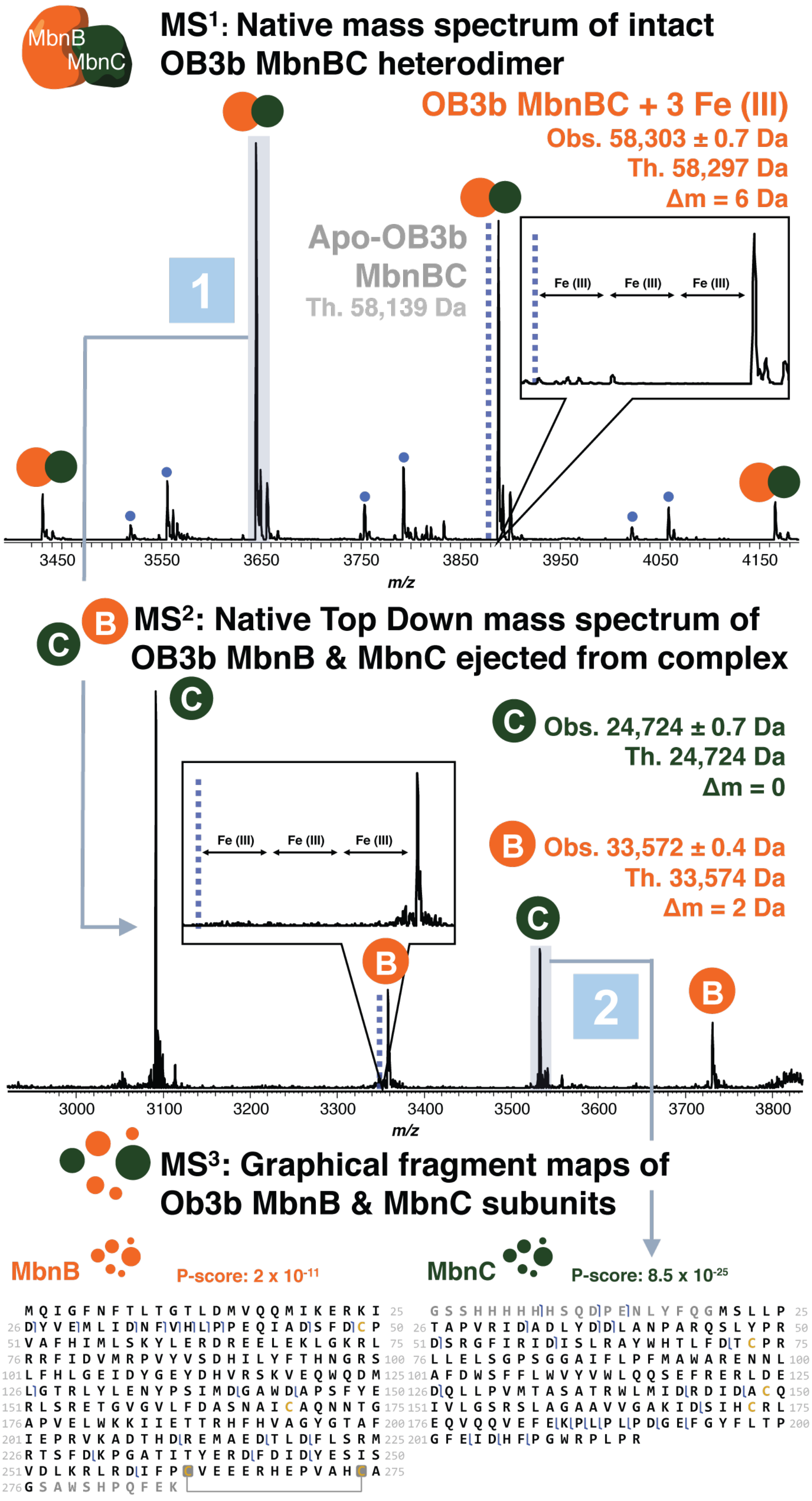
MbnB
MbnC
MS^1: Native mass spectrum of intact OB3b MbnBC heterodimer
OB3b MbnBC + 3 Fe (III)
Obs. 58,303 ± 0.7 Da
Th. 58,297 Da
Δm = 6 Da
Apo-OB3b MbnBC
Th. 58,139 Da
1
Fe (III)
Fe (III)
Fe (III)
3450
3550
3650
3750
3850
3950
4050
4150
m/z
B
C
MS^2: Native Top Down mass spectrum of OB3b MbnB & MbnC ejected from complex
C
C Obs. 24,724 ± 0.7 Da
Th. 24,724 Da
Δm = 0
B Obs. 33,572 ± 0.4 Da
Th. 33,574 Da
Δm = 2 Da
Fe (III)
Fe (III)
Fe (III)
B
C
2
B
3000
3100
3200
3300
3400
3500
3600
3700
3800
m/z
MS^3: Graphical fragment maps of Ob3b MbnB & MbnC subunits
MbnB
P-score: 2 x 10^{-11}
MbnC
P-score: 8.5 x 10^{-25}
M Q I G F N F T L T G T L D M V Q Q M I K E R K I 25
26 D Y V E M L I D N F V H L P P E Q I A D S F D C P 50
51 V A F H I M L S K Y L E R D R E E L E K L G K R L 75
76 R R F I D V M R P V Y Y V S D H I L Y F T H N G R S 100
101 L F H L G E I D Y G E Y D H V R S K V E Q W Q D M 125
126 L G T R L Y L E N Y P S I M D G A W D A P S F Y E 150
151 R L S R E T G V G V L F D A S N A I C A Q N N T G 175
176 A P V E L W K K I I E T T R H F H V A G Y G T A F 200
201 I E P R V K A D T H D R E M A E D T L D F L S R M 225
226 R T S F D K P G A T I T Y E R D F D I D Y E S I S 250
251 V D L K R L R D I F P C V E E E R H E P V A H C A 275
276 G S A W S H P Q F E K
G S S H H H H H H S Q D P E N L Y F Q G M S L L P 25
26 T A P V R I D A D L Y D D L A N P A R Q S L Y P R 50
51 D S R G F I R I D I S L R A Y W H T L F D T C P R 75
76 L L E L S G P S G G A I F L P F M A W A R E N N L 100
101 A F D W S F F L W V Y V W L Q Q S E F R E R L D E 125
126 D Q L L P V M T A S A T R W L M I D R D I D A C Q 150
151 I V L G S R S L A G A A V V G A K I D S I H C R L 175
176 E Q V Q Q V E F E K P L P L P D G E F G Y F L T P 200
201 G F E I D H F P G W R P L P R

Fig. S6. Native top down mass spectrometry (nTDMS) performed on MbnBC from *Ms. trichosporium* OB3b localizes metal loading to MbnB.

The nTDMS platform employed includes the analysis of the intact protein complex (MS^1, top panel), which provides the total mass (reported as a neutral average mass value). The theoretical and observed molecular weights for MbnBC containing three Fe(III) ions are indicated in orange. The theoretical molecular weight of apo MbnBC is indicated in gray and denoted on the spectrum with a dotted blue line. In stage two, the complex is collisionally activated with nitrogen gas to eject monomers (MS^2, middle panel), as shown by the blue arrow in step 1, thereby liberating the subunits that comprise each intact complex. In stage three, further vibrational activation of the ejected subunits via collisions with neutral gas, as shown by the arrow in step 2, yields backbone fragmentation products from each monomer (MS^3, bottom panel). These fragment ions are depicted as blue flags in the graphical fragment maps of the lower panel, indicating which regions of the protein sequence are accounted for in mass by fragmentation. Blue dots denote unidentified proteins or contaminants in the sample.

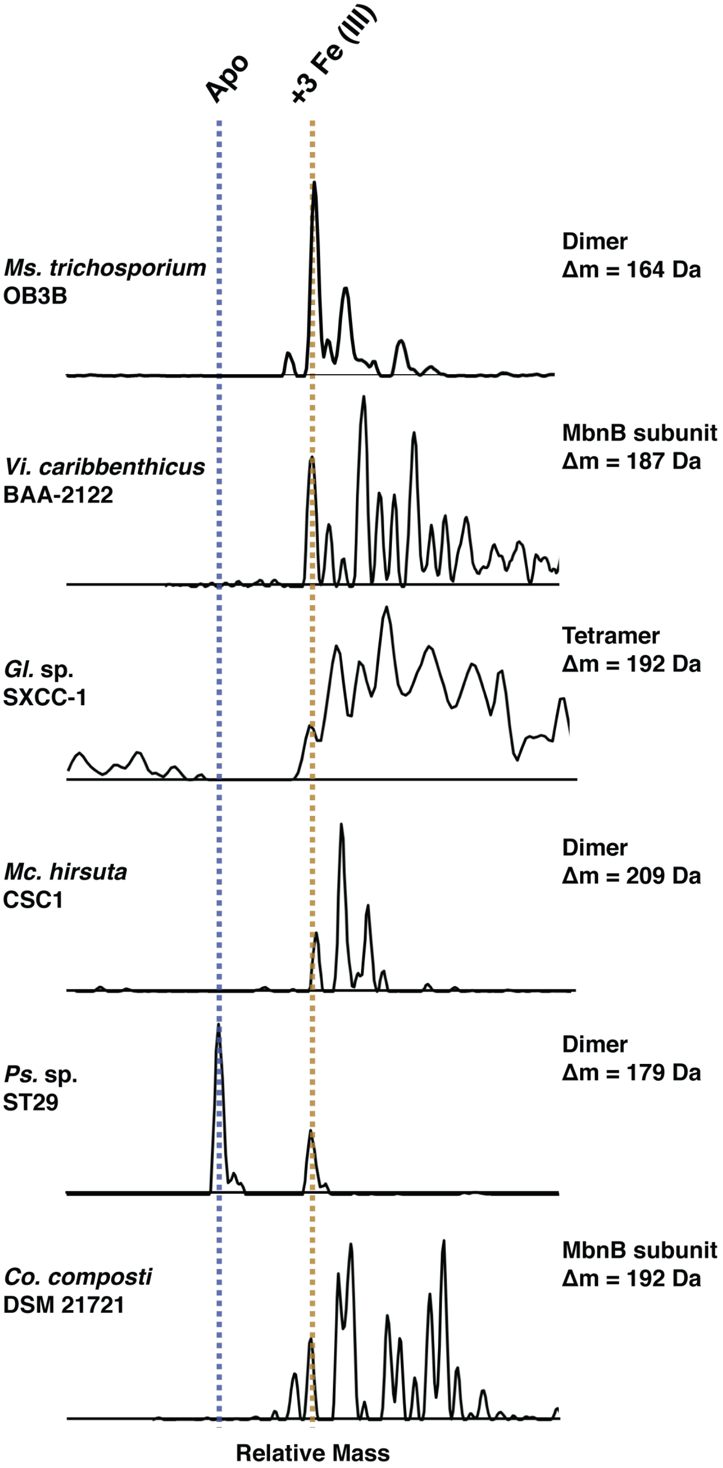

Fig. S7. MS^1 measurements of MbnBC complexes from various species consistently localize metal loading to MbnB.

All MbnBC complexes were investigated as described in **Fig. S6**. Although all complexes except for that of *Gl*. sp. SXCC-1 MbnBC are present as heterodimers based on size exclusion chromatography, observed oligomers with MbnB components include MbnBC heterodimers (*Ms. trichosporium* OB3B, *Mc. hirsuta* CSC1, and *Ps.* sp. ST29), MbnB monomers (*Vi. caribbenthicus* BAA-2122, *Co. composti* DSM 21721), and an $(MbnBC)_2$ tetramer (*Gl.* sp. SXCC-1) that yield observed mass shifts from the theoretical masses (Δm) that are consistent within <5 Da with the mass shift associated with the presence of three Fe (III) ions (Δm of 158.5 Da).

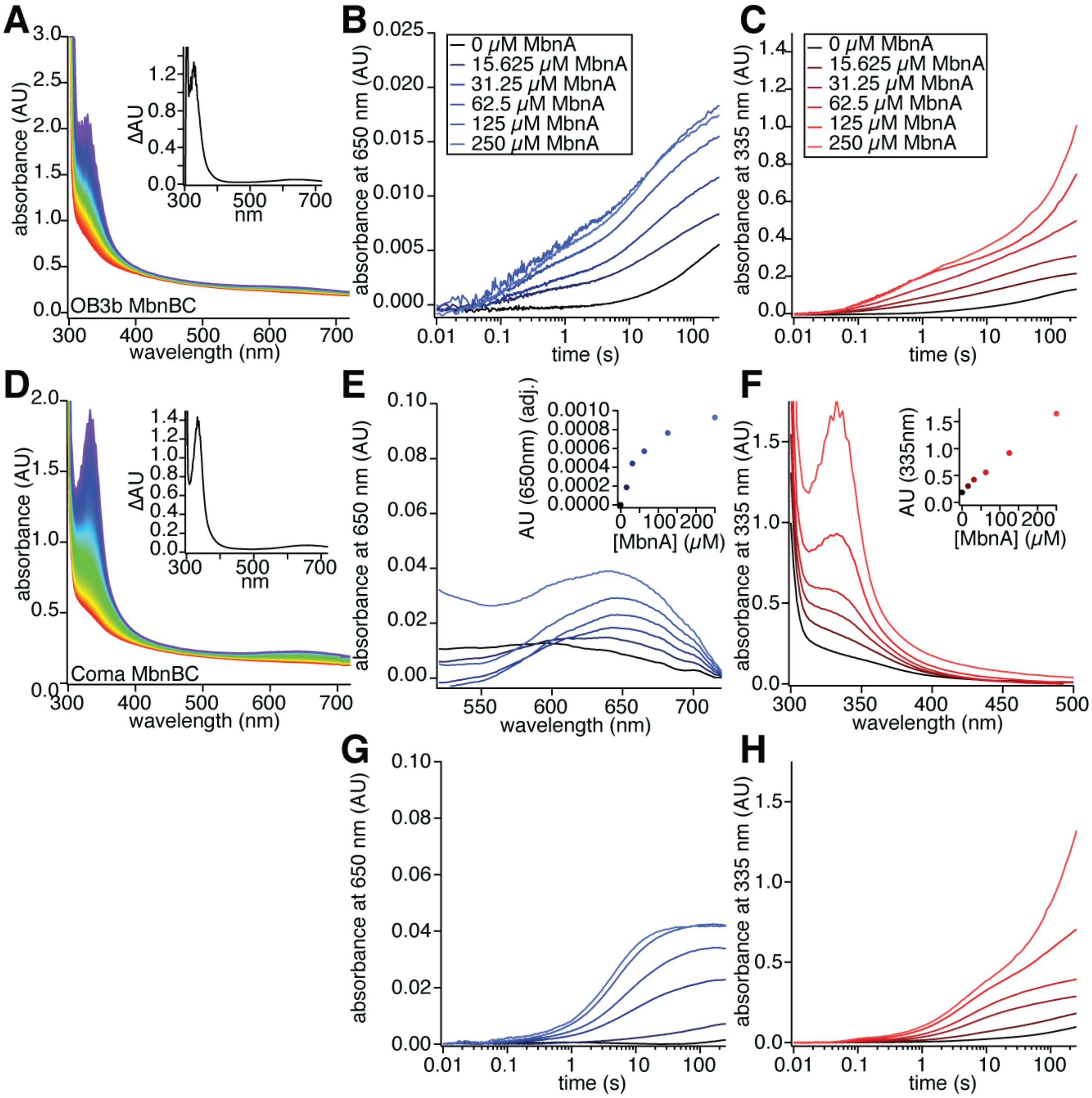

Fig. S8. Similar reactivity of *Ms. trichosporium* OB3b MbnBC and *Co. composti* DSM 21721 MbnBC with *Ms. trichosporium* OB3b MbnA.

(**A**) Spectra collected over 250 s following the mixing of 100 µM *Ms. trichosporium* OB3b MbnBC, 250 µM *Ms. trichosporium* OB3b MbnA, and 900 µM O_2 (also shown in Fig. 3A, but included here for reference). Inset spectrum is a difference spectrum between the final and initial timepoints. (**B, C**) Formation of the 650 nm feature (**B**) and the 335 nm feature (**C**) over 250 s at different concentrations of MbnA. As with reactions carried out under a range of O_2 concentrations (**Fig. S9C**), a notable difference in the shape of the curves at 335 nm is observed between the addition of 31.25 and 62.5 µM MbnA. This change, which results in a comparatively linear curve (rather than an exponential curve), can be attributed to steady-state product formation by MbnBC, and indicates that the concentration of the active metal cofactor required to achieve steady-state product formation is between 31.25 and 62.5 µM. (**D**) Spectra acquired over 250 s following the reaction of 100 µM *Co. composti* DSM 21721 MbnBC (1.1 equivalents of iron per heterodimer) with 250 µM *Ms. trichosporium* OB3b MbnA and 900 µM O_2. Inset: Difference spectrum calculated via the subtraction of the initial spectrum from the final spectrum. The reactivity is very similar to that observed for *Ms. trichosporium* OB3b reacting with its cognate substrate. (**E**) Endpoint spectra of the 650 nm feature at various MbnA concentrations. Inset: Adjusted maxima for 650 nm feature at different MbnA concentrations following a dropline correction of the baseline (using values at 640 and 660 nm). The amplitude of this feature increases with increasing concentrations until MbnA is in excess of MbnBC; saturation is observed after this point. (**F**) Endpoint spectra of the 335 nm feature at various MbnA concentrations. Inset: Maxima for the 335 nm feature at different MbnA concentrations. As observed for *Ms. trichosporium* OB3b MbnBC, the amplitude of this feature increases with increasing amounts of MbnA. (**G**, **H**) Kinetic traces reflecting the formation of the 650 nm (**G**) and 335 nm (**H**) features over 250 s at different concentrations of MbnA and excess O_2. The 335 nm feature begins to exhibit steady-state behavior between 15.625 and 31.25 µM MbnA, suggesting that the concentration of the active cofactor in the *Co. composti* DSM 21721 MbnBC falls within this range.

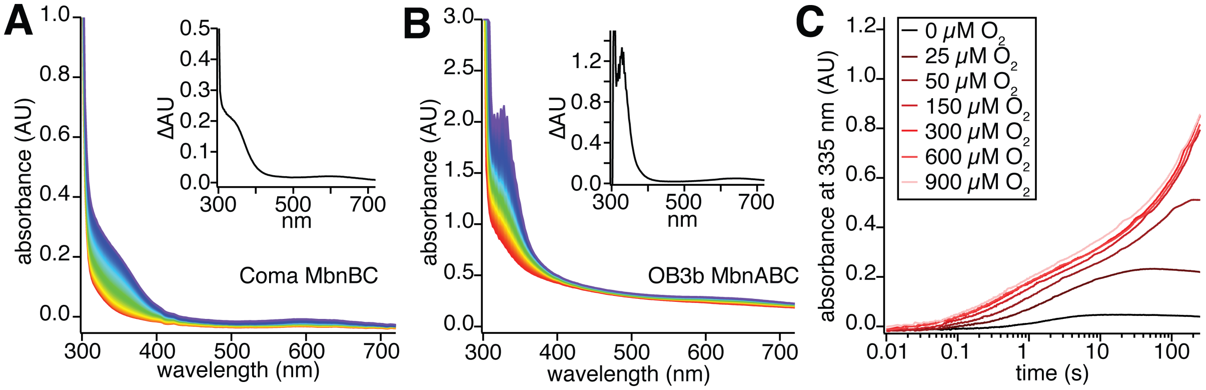

Fig. S9. Reaction of *Co. composti* DSM 27121 MbnBC and of *Ms. trichosporium* OB3b MbnBC with O_2 and with *Ms. trichosporium* OB3b MbnA

(**A**) Formation of a feature at ~350 nm over 250 s after the addition of oxygen-saturated buffer to 100 µM *Co. composti* DSM 21721 MbnBC containing 1.1 equivalents of iron. Inset: Difference spectrum obtained by subtracting the final spectrum from the initial spectrum. (**B**) Reaction of 100 µM *Ms. trichosporium* OB3b MbnBC with 125 µM *Ms. trichosporium* OB3b MbnA and 900 µM O_2, monitored over 25 s (also shown in Fig. 3A, but included here for reference). (**C**) Kinetic traces at 335 nm obtained after a reaction between 100 µM *Ms. trichosporium* OB3b MbnBC (1.4 Fe/heterodimer) and 125 µM *Ms. trichosporium* OB3b MbnA in the presence of different concentrations of oxygen. These traces reflect the oxygen dependence of the peptide-associated feature (335 nm). A notable difference in the kinetic traces is observed between 25 and 50 µM O_2, which could reflect a crossover from O_2 consumption in order to generate an active cofactor and O_2 consumption to form product (modified MbnA) or from a single substrate turnover to multiple turnovers.

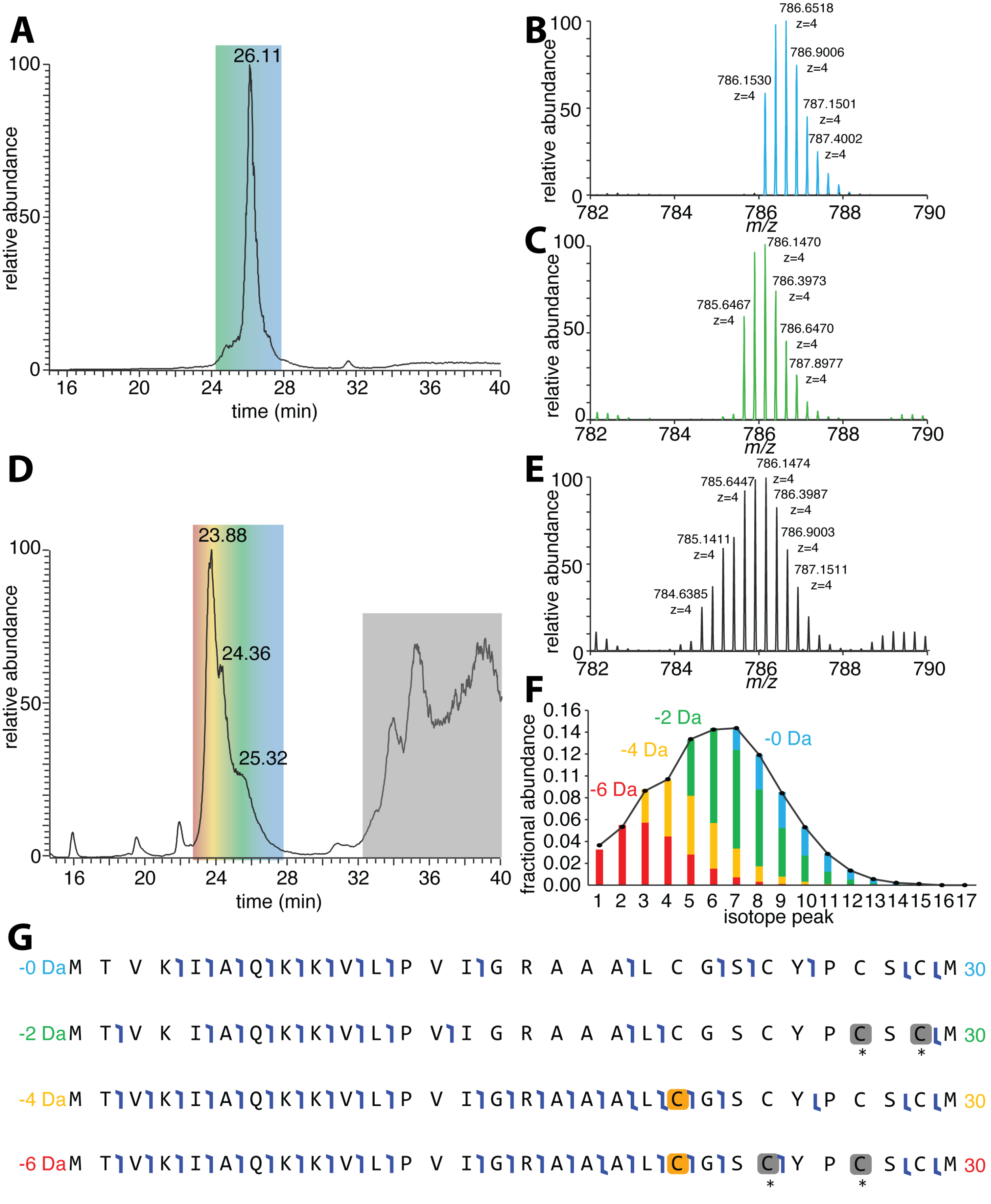

Fig. S10. Mass spectrometric analysis of MbnA modified by MbnBC from *Ms. trichosporium* OB3b.

(**A**) Total ion chromatogram of MbnA starting material. The major peak at 26.11 min is unmodified MbnA (blue, mass spectrum in **B**), while the shoulder at the earlier retention time represents an MbnA species 2.014 Da lighter (-2H, in green, mass spectrum in **C**). (**D**) Total ion chromatogram of MbnA modified by MbnBC. Species with a gray background represent signals from MbnB and MbnC. Species with a multicolored background represent the mixed species of MbnA present, including unmodified and -2H, as described above, but also -4H (-4.031 Da) in yellow, and -6H (-6.047 Da) in red. (**E**) Representative mixed mass spectrum obtained by averaging scans from 23-28 minutes in **D**. (**F**) Fit of the observed mass spectrum in E to a simple mixture of the 4 species described above. Species are present in an apparent ratio of 0.07:0.37:0.25:0.31 unmodified: -2H: -4H: -6H. (**G**) Tandem MS fragmentation maps of the 4 species obtained by higher energy collisional dissociation. Colors represent the same species as noted in **D**. Fragment ions are noted as “flags” between amino acids with left-pointing angles above the flag indicating N-terminal ions and right-pointing angles below the flag indicating C-terminal ions. Cysteines colored in orange report on a -4.031 Da shift applied to that cysteine, while cysteines colored in gray are posited to be part of a disulfide linkage. Disulfides in the -2H and -6H species are likely mixed structural isomers involving any of the remaining unmodified cysteines, based on MS^2 fragmentation information.

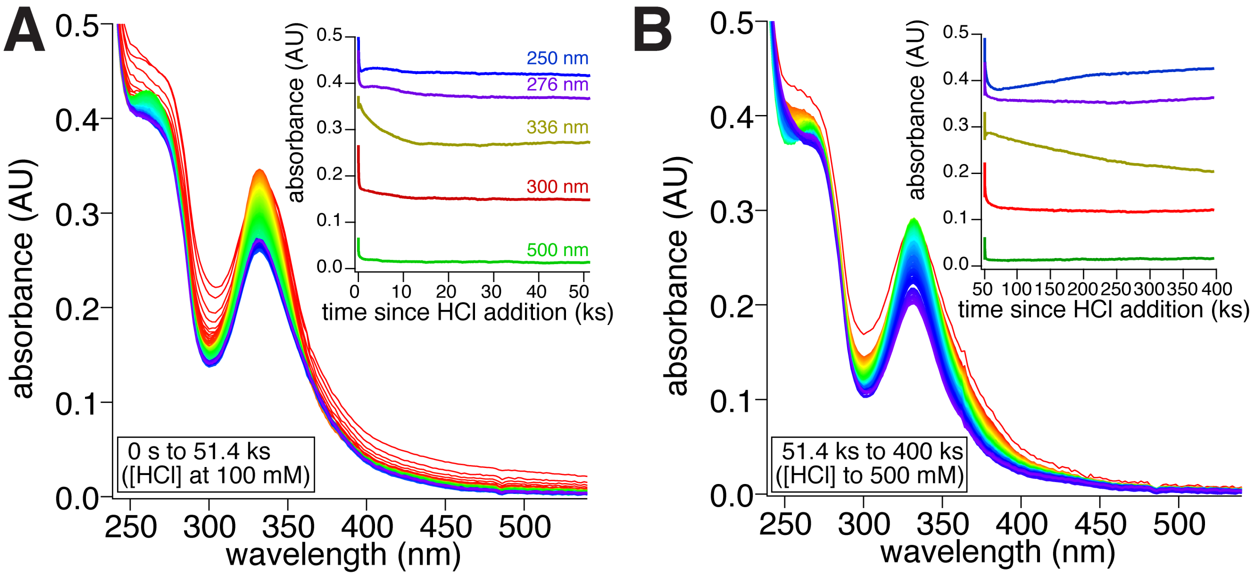

Fig. S11. Acid hydrolysis of modified *Ms. trichosporium* OB3b MbnA.

(**A**) UV-vis spectra over the first 14 h after addition of hydrochloric acid to 100 mM. Inset: absorbance at specific wavelengths of interest. (**B**) UV-vis spectra of modified MbnA exposed to hydrochloric acid over 4 d after an increase of the acid concentration to 500 mM.

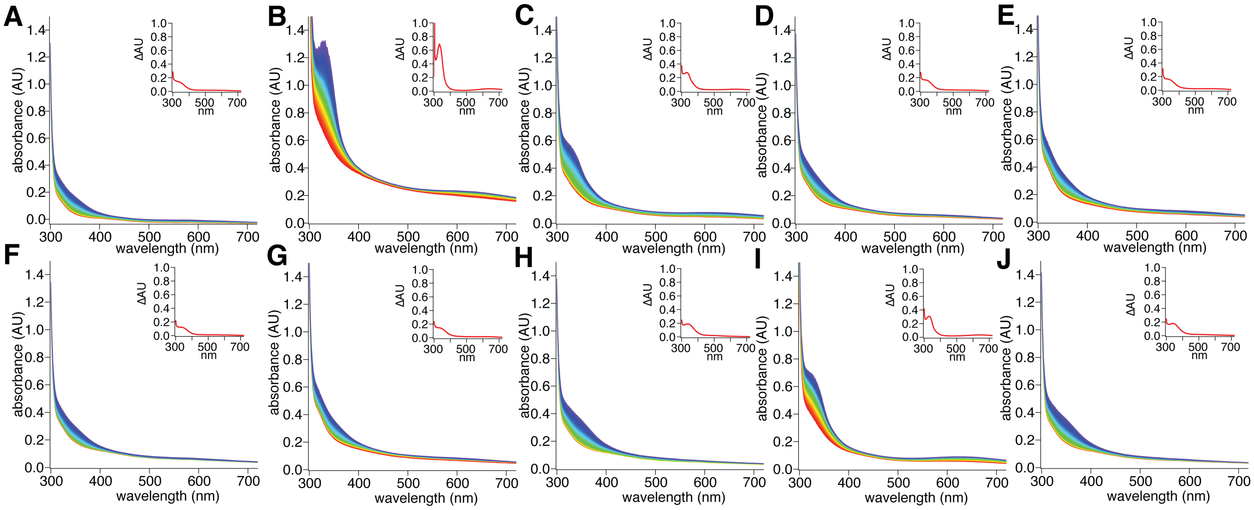

Fig. S12. Reaction of 100 µM anaerobic *Ms. trichosporium* OB3b MbnBC (1.4 equivalents of iron per heterodimer) with 125 µM *Ms. trichosporium* OB3b MbnA variants in the presence of 900 µM O_2 over 250 s.

(**A**) Control without MbnA. (**B**) Wild-type MbnA. (**C**) $\text{MbnA}_{9\text{-}30}$, in which the first set of conserved lysines are absent from the leader peptide. (**D**) $\text{MbnA}_{15\text{-}30}$, in which the first two sets of conserved lysines/arginines are absent from the leader peptide. (**E**) $\text{MbnA}_{\text{core}}$, missing the leader peptide. (**F**) $\text{MbnA}_{\text{leader}}$, missing the core peptide. (**G**) $\text{MbnA}_{\text{leader,core}}$, in which the leader and core peptides are added together *in trans*. (**H**) $\text{MbnA}_{\text{C21S}}$, in which the cysteine in the first modification moiety is replaced by a serine. (**I**) $\text{MbnA}_{\text{C27S}}$, in which the cysteine in the second modification moiety is replaced by a serine. (**J**) $\text{MbnA}_{\text{C21,27S}}$, in which both cysteines in both modification moieties are replaced by serines.

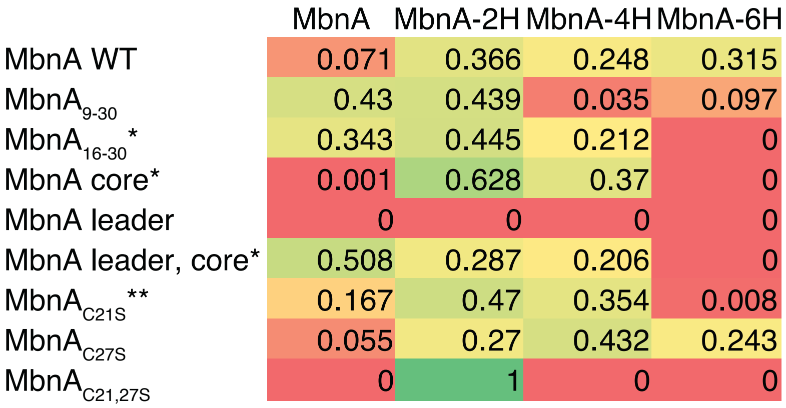

	MbnA	MbnA-2H	MbnA-4H	MbnA-6H
MbnA WT	0.071	0.366	0.248	0.315
MbnA$_{9\text{-}30}$	0.43	0.439	0.035	0.097
MbnA$_{16\text{-}30}$*	0.343	0.445	0.212	0
MbnA core*	0.001	0.628	0.37	0
MbnA leader	0	0	0	0
MbnA leader, core*	0.508	0.287	0.206	0
MbnA$_{C21S}$**	0.167	0.47	0.354	0.008
MbnA$_{C27S}$	0.055	0.27	0.432	0.243
MbnA$_{C21,27S}$	0	1	0	0

Fig. S13. Mass spectrometry analysis heat map for *Ms. trichosporium* OB3b MbnA variants modified by MbnBC from *Ms. trichosporium* OB3b.

Heat map showing analysis of mixed MbnA MS^1 species present when reacting MbnA variants listed on the left with MbnBC as was performed in **Fig. S10F**. Only MbnA wild-type (WT), MbnA$_{9\text{-}30}$ and MbnA$_{C27S}$ showed *bona fide* conversion of C21 to the oxazolone species by tandem MS. Fragmentation of species marked with * indicate mixed disulfide species present and species marked with ** show an identical mass spectrum to that of the starting material. All reactions were analyzed in the absence of reductant, accounting for the presence of some -4 Da shifts that correspond to double disulfide formation in unmodified peptides, rather than authentic peptide modification.

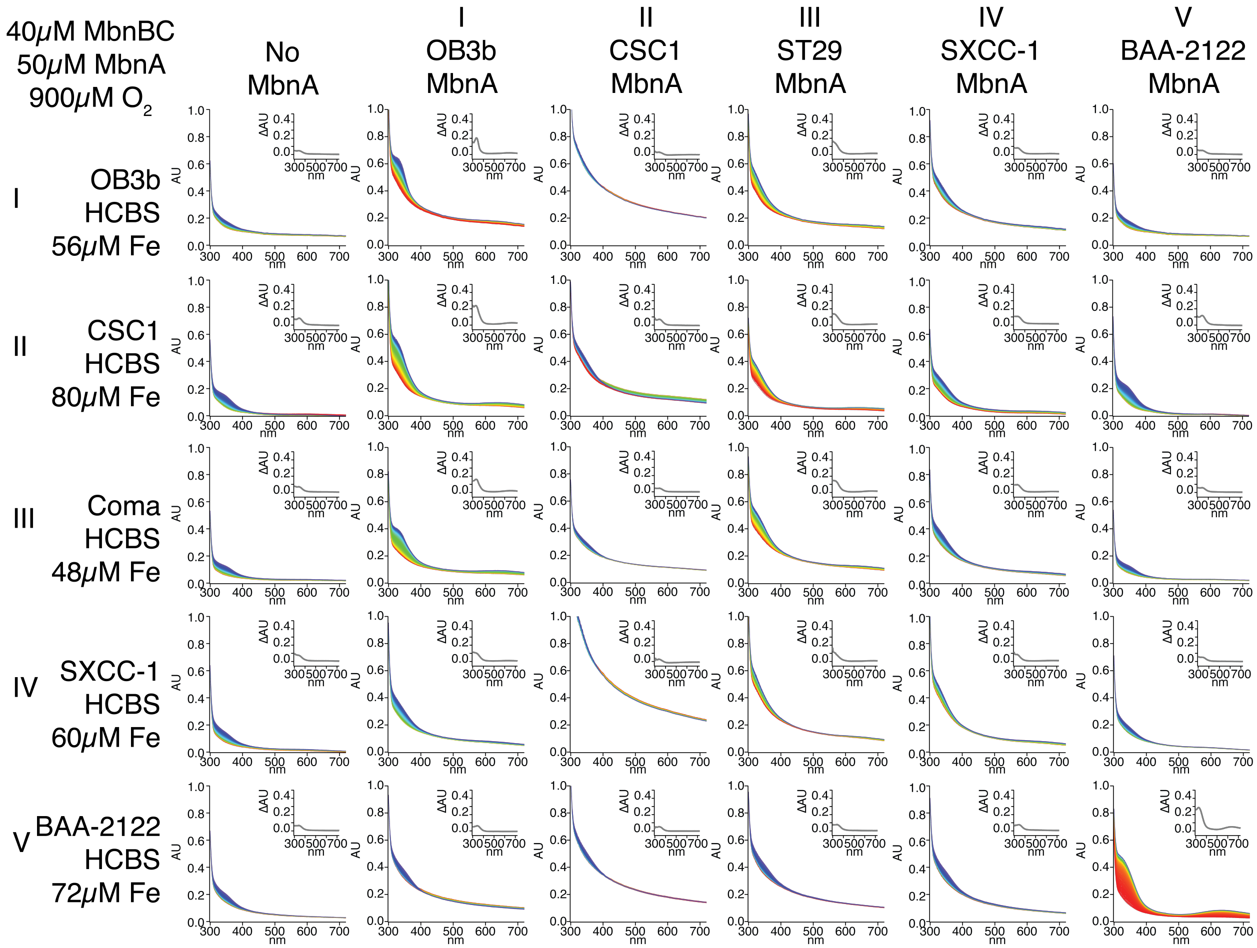

Fig. S14. Reaction of MbnBCs from five Mbn groups (*Ms. trichosporium* OB3b (Group I), *Mc. hirsuta* CSC1 (Group IIa), *Co. composti* DSM 27171 (Group III), *Gl.* Sp. SXCC-1 (Group IV), and *Vi. caribbenthicus* BAA-2122 (Group V)) with MbnAs from five Mbn groups (*Ms. trichosporium* OB3b (Group I), *Mc. hirsuta* CSC1 (Group IIa), *Ps.* Sp. ST29 (Group III), *Gl.* Sp. SXCC-1 (Group IV), and *Vi. caribbenthicus* BAA-2122 (Group V).)

In all figures, the inset shows the difference spectrum between the final (250 s) and the starting spectra. Due to solubility issues, no reliable activity was observed for the *Mc. hirsuta* CSC1 MbnA peptide when added to any MbnBC complex. Otherwise, all MbnBC complexes from Groups I-IV exhibited at least a small level of reactivity with all MbnAs from Groups I-IV, as determined by the formation of 335 and 650 nm features over the course of the reaction. Precise maxima vary by species. Group V MbnA and MbnBC are exclusively compatible with each other. Iron equivalents per heterodimer are as follows: 1.4 (*Ms. trichosporium* OB3b), 2.0 (*Mc. hirsuta* CSC1), 1.2 (*Co. composti* DSM 21721), 1.5 (*Gl.* sp. SXCC-1), and 1.8 (*Vi. caribbenthicus* BAA-2122).

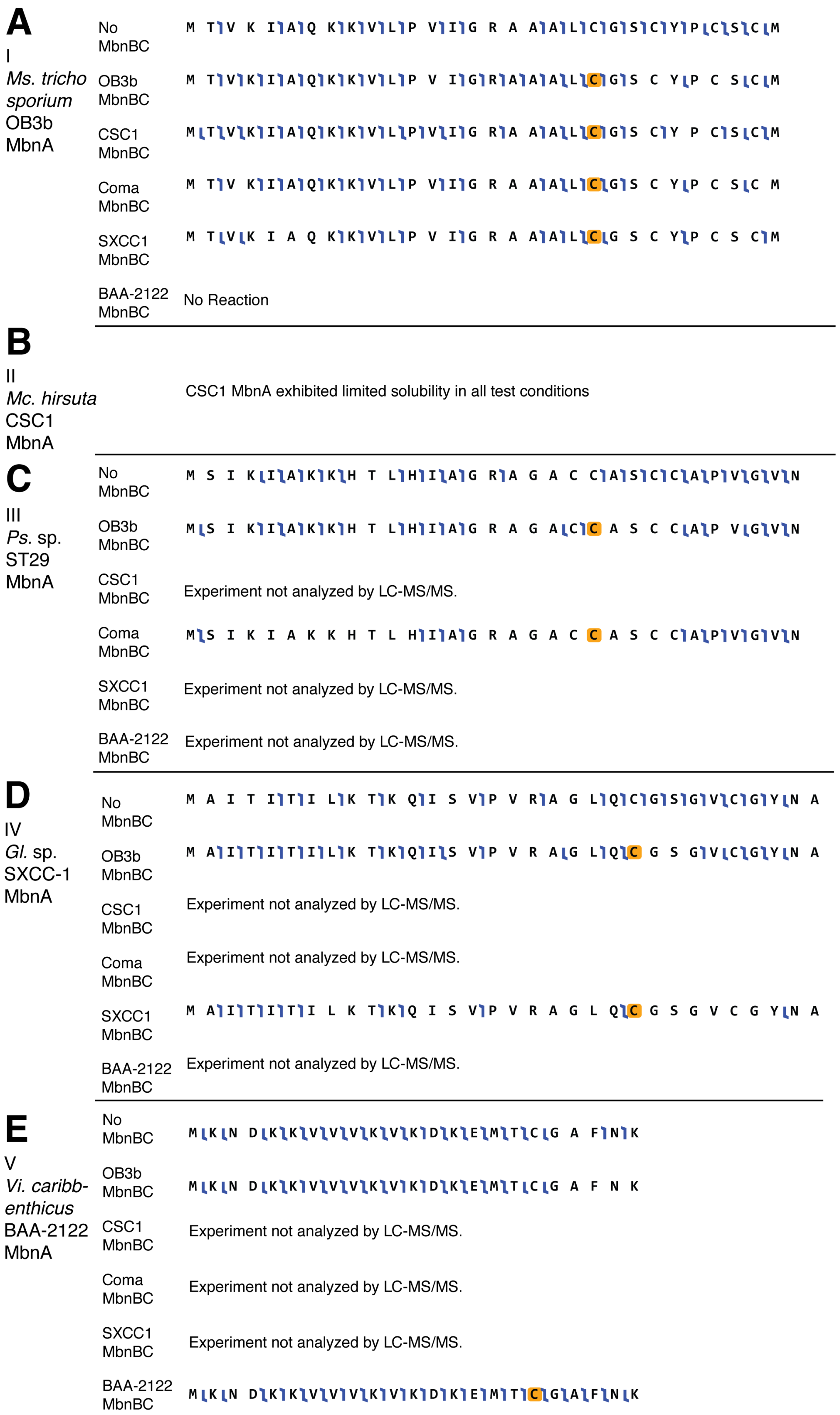
A
I
Ms. tricho sporium
OB3b
MbnA
No MbnBC
M T V K I A Q K K V L P V I G R A A A L C G S C Y P C S C M
OB3b MbnBC
M T V K I A Q K K V L P V I G R A A A L C G S C Y P C S C M
CSC1 MbnBC
M T V K I A Q K K V L P V I G R A A A L C G S C Y P C S C M
Coma MbnBC
M T V K I A Q K K V L P V I G R A A A L C G S C Y P C S C M
SXCC1 MbnBC
M T V K I A Q K K V L P V I G R A A A L C G S C Y P C S C M
BAA-2122 MbnBC
No Reaction
B
II
Mc. hirsuta
CSC1
MbnA
CSC1 MbnA exhibited limited solubility in all test conditions
C
III
Ps. sp.
ST29
MbnA
No MbnBC
M S I K I A K K H T L H I A G R A G A C C A S C C A P V G V N
OB3b MbnBC
M S I K I A K K H T L H I A G R A G A C C A S C C A P V G V N
CSC1 MbnBC
Experiment not analyzed by LC-MS/MS.
Coma MbnBC
M S I K I A K K H T L H I A G R A G A C C A S C C A P V G V N
SXCC1 MbnBC
Experiment not analyzed by LC-MS/MS.
BAA-2122 MbnBC
Experiment not analyzed by LC-MS/MS.
D
IV
Gl. sp.
SXCC-1
MbnA
No MbnBC
M A I T I T I L K T K Q I S V P V R A G L Q C G S G V C G Y N A
OB3b MbnBC
M A I T I T I L K T K Q I S V P V R A G L Q C G S G V C G Y N A
CSC1 MbnBC
Experiment not analyzed by LC-MS/MS.
Coma MbnBC
Experiment not analyzed by LC-MS/MS.
SXCC1 MbnBC
M A I T I T I L K T K Q I S V P V R A G L Q C G S G V C G Y N A
BAA-2122 MbnBC
Experiment not analyzed by LC-MS/MS.
E
V
Vi. caribbenthicus
BAA-2122
MbnA
No MbnBC
M K N D K K V V V K V K D K E M T C G A F N K
OB3b MbnBC
M K N D K K V V V K V K D K E M T C G A F N K
CSC1 MbnBC
Experiment not analyzed by LC-MS/MS.
Coma MbnBC
Experiment not analyzed by LC-MS/MS.
SXCC1 MbnBC
Experiment not analyzed by LC-MS/MS.
BAA-2122 MbnBC
M K N D K K V V V K V K D K E M T C G A F N K

Fig. S15. Representative LC-MS-MS fragmentation maps showing promiscuous reactivity of MbnBC enzymes with MbnA peptide substrates from various species.

These reactions correspond to the UV-vis spectra in **Fig. S14**, though not all reactions from that figure are analyzed here. Fragment ions are noted as “flags” between amino acids with left-pointing angles above the flag indicating N-terminal ions and right-pointing angles below the flag indicating C-terminal ions. Cysteines highlighted in orange indicate a -4.031 Da shift applied to that cysteine. (**A**) Fragmentation maps corresponding to major species present in reactions involving MbnA from *Ms. trichosporium* OB3b (Group I). (**B**) No reactions were observed with MbnA from *Mc. hirsuta* CSC1 (Group IIa) due to limited solubility of this peptide. (**C**) Fragmentation maps corresponding to major species present in reactions involving MbnA from *Ps.* sp. ST29 (Group III). (**D**) Fragmentation maps corresponding to major species present in reactions involving MbnA from *Gl.* sp. SXCC-1 (Group IV) and (**E**) Fragmentation maps corresponding to major species present in reactions with MbnA from *Vi. caribbenthicus* BAA-2122 (Group V).

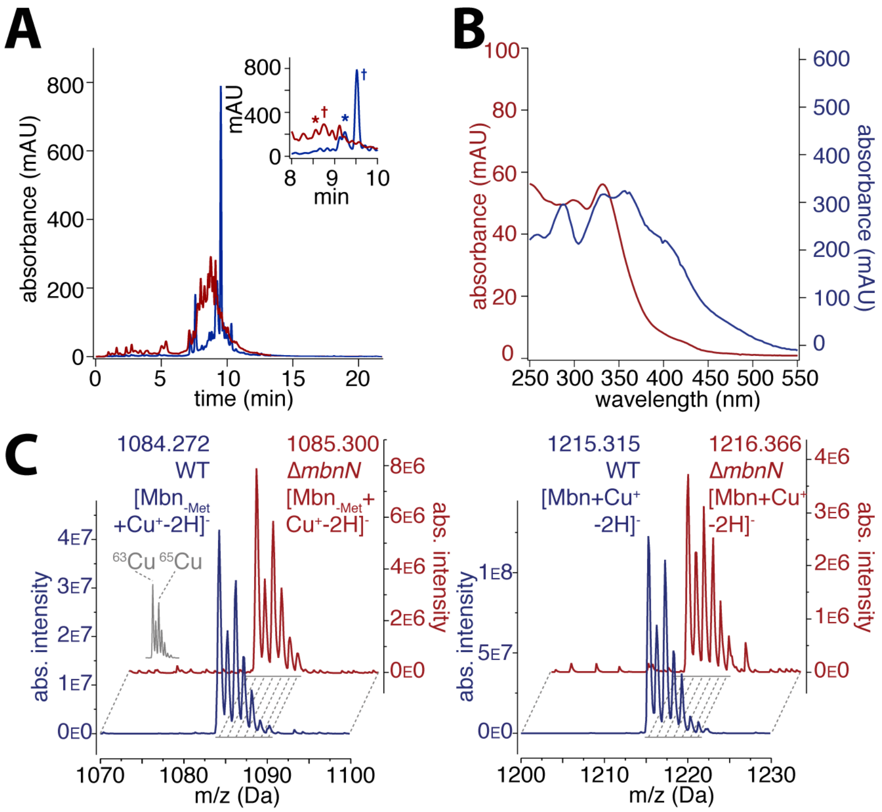

Fig. S16. Mbn produced by the Δ*mbnN* strain does not undergo the N-terminal transamination reaction, altering the mass and absorption features.

(**A**) Elution points for full-length Mbns are indicated with a cross (WT in blue and Δ*mbnN* in red) while Mbns lacking the C-terminal methionine are indicated with an asterisk (WT in blue and Δ*mbnN* in red). (**B**) UV-vis spectrum of *Ms. trichosporium* OB3b WT (blue) and Δ*mbnN* (red) CuMbn. In the absence of extended conjugation, the features at λ_{max} 360 nm and 400 nm are absent in the holo compound produced by the Δ*mbnN* strain. (**C**) LC-MS of *Ms. trichosporium* OB3b WT (blue) and Δ*mbnN* (red) CuMbn. Left: Mbn missing the C-terminal methionine. Right: full-length Mbn. In both forms, a 1 Da increase in mass is observed in the knockout strain, consistent with an "N-terminal" amine rather than a carbonyl group. A previously reported knockout of the same gene produced a compound with a neutral mass of 999.46 Da (based on some of the provided data) or a neutral mass of 998.26 Da (based on the structure), which was attributed to an apo Mbn intermediate exhibiting complete formation of Oxa_B and incomplete formation of Oxa_A combined with the presence of an N-terminal amine, and C-terminal methionine loss (*62*). However, given the increased acid lability exhibited by the Mbn intermediate (and the masses observed in the copper-stabilized sample), a more likely explanation for this species would be complete formation of Oxa_A and Oxa_B in the Mbn intermediate shown in Fig. 5, combined with loss of the C-terminal methionine and acid hydrolysis of Oxa_A, which results in a well attested mass loss (*13*, *24*). The resulting compound would be predicted to have an exact mass of 998.28, or $[M+H]^+$ of 999.28.

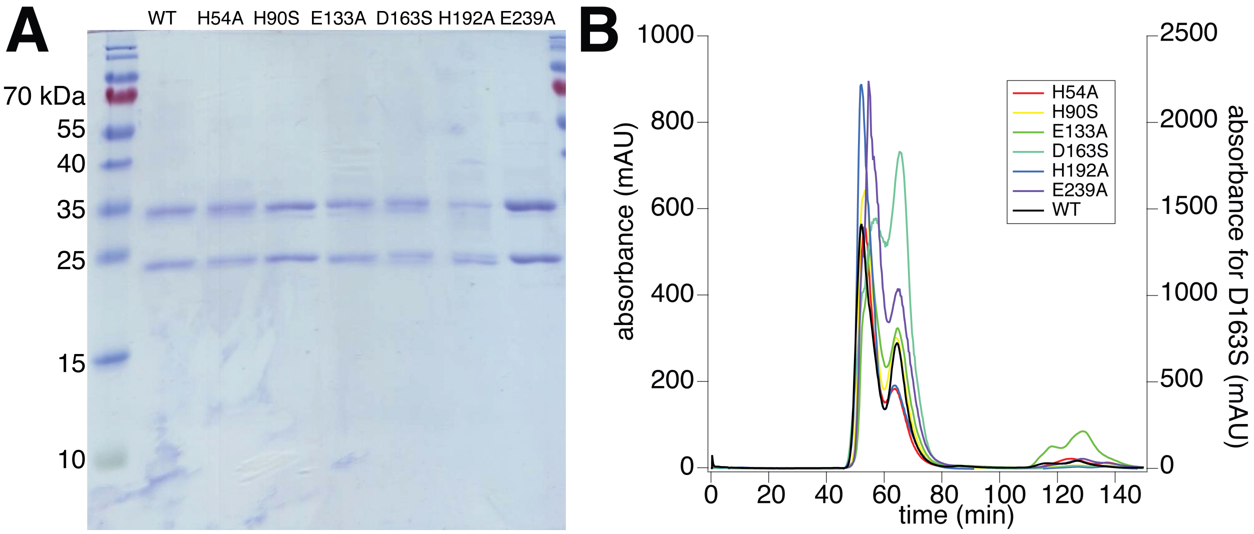

Fig. S17. Mutagenesis of proposed MbnB iron ligands in *Ms. trichosporium* OB3b MbnBC. (**A**) SDS-PAGE of MbnBC complexes with site-specific mutations in MbnB (H54A, H90S, E133A, D163S, H192A, and E239A). (**B**) Chromatograms (at 280 nm) for both wild-type and variant complexes, as purified on a Superdex 75 gel filtration column. The first major peak corresponds to the void volume (and sometimes to a Ni-binding contaminant protein); the second major peak at 65 min corresponds to the heterodimeric MbnBC complex. All variants still form a heterodimer.

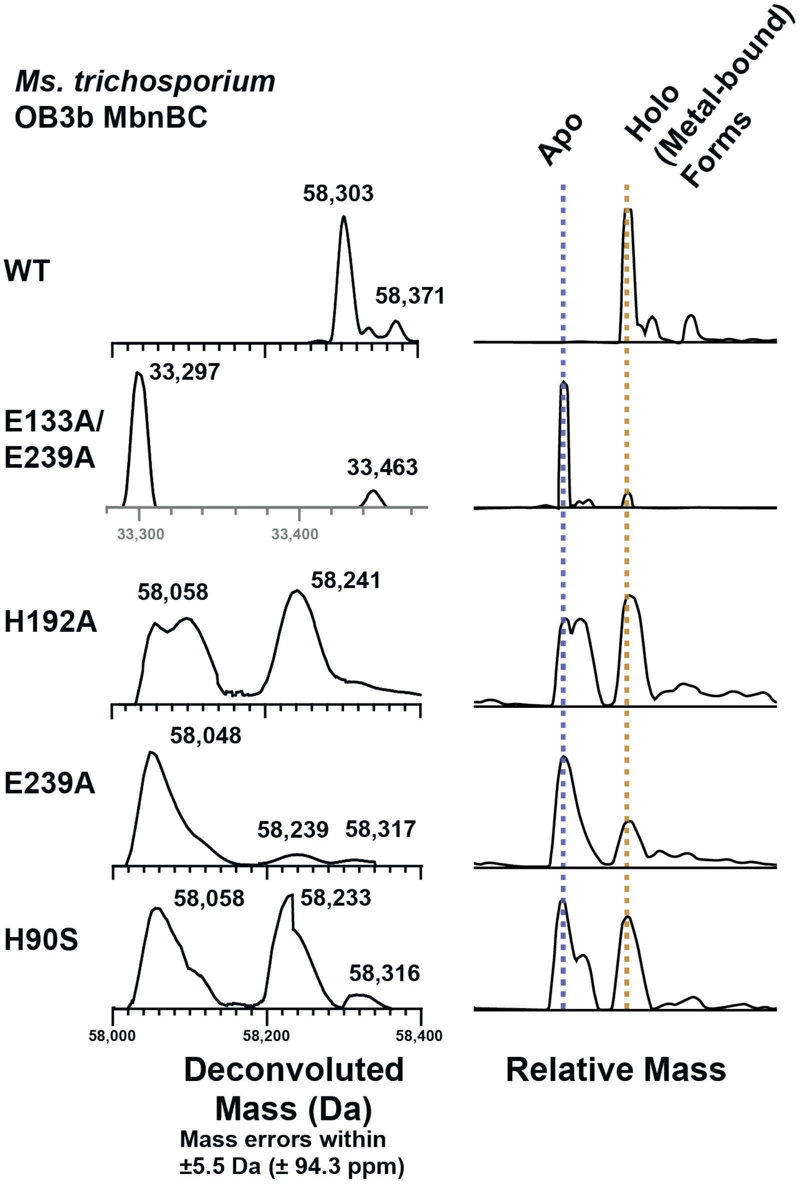

Fig. S18. MS^1 measurements of variant MbnBC complexes support reduced metal loading of MbnB.

All experiments were carried out as described in Fig. S6. Specific point mutations to metal binding residues in MbnB resulted in the loss or reduction of metal binding observed by nTDMS. Not all variants produced usable MS^2 data. The left panels are labeled with the deconvoluted masses of the intact mutant heterodimers. Only monomeric MbnB was observed in MS^1 data for the E133A/E239A double mutant, although polyacrylamide gel electrophoresis and size exclusion chromatography indicated that the protein complex is isolated as an MbnBC heterodimer. Excerpted sections from raw spectra MS^1 spectra are presented on the right panels, centered around the theoretical mass of the apo MbnBC complex or MbnB subunit, indicating mass changes when compared to the wild-type enzymes (in Fig. S6 and Fig. S7) that correspond to the loss of metal binding due to the indicated point mutations.

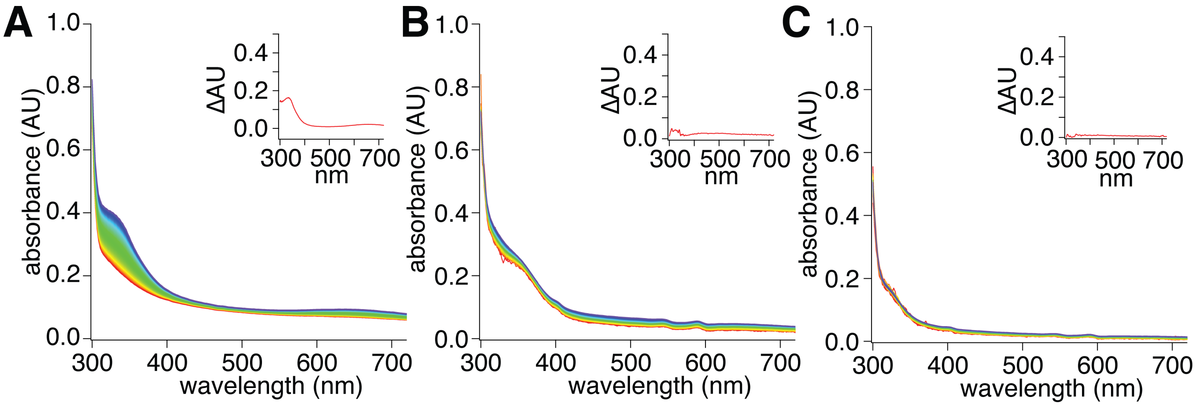

Fig. S19. Chelation or oxidation of the iron site eradicates MbnABC reactivity.

(**A**) Reaction of 40 μM anaerobic MbnBC, 50 μM MbnA, and 900 μM O_2. (**B**) Reaction of 40 μM MbnBC, 50 μM MbnA, and 900 μM O_2 over 250 s for MbnBC oxidized by 20-fold excess H_2O_2, with protein recovery via a Superdex 75 size exclusion column. Consistent with complete iron oxidation, the broad 300-400 nm feature is visible, but no 335 nm feature associated with peptide modification grows in over time. (**C**) Reaction of 40 μM MbnBC with 50 μM MbnA in the presence of 900 μM O_2 after ferrozine chelation of iron from dithionite-reduced MbnBC, followed by MbnBC recovery via Superdex 75 size exclusion column. Neither features associated with iron oxidation nor with peptide modification or protein-peptide interactions are observed.

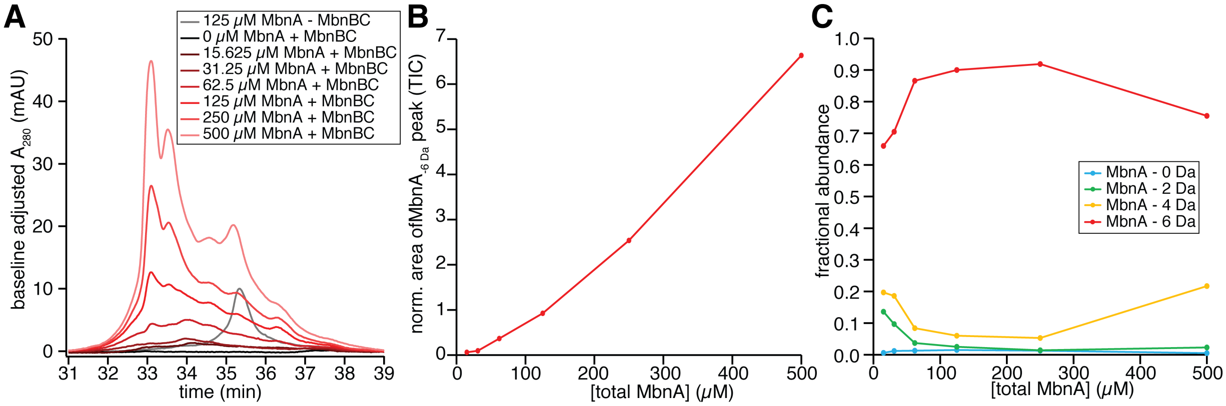

Fig. S20. Mass spectrometry confirms that MbnBC is achieving multiple turnovers during MbnA modification.

(**A**) 280 nm chromatograms showing elution peaks for reduced samples at varying concentrations of *Ms. trichosporium* OB3b MbnA after reaction with 100 µM *Ms. trichosporium* OB3b MbnBC in the presence of excess oxygen. Modified MbnA elutes earlier; the main peaks at 33 min and 35.5 min represent the fully modified and unmodified peptide without any additional disulfides, and additional peaks contain at least one disulfide. (**B**) Normalized area under total ion current peaks assigned to the -6 Da feature of the modified peptide. (**C**) Fractional abundance of modified and unmodified species. In samples with significant re-oxidation, the -4 Da shift is dominated by peptide containing two intramolecular disulfides, and the -6 Da shift represents most of the modified peptide.

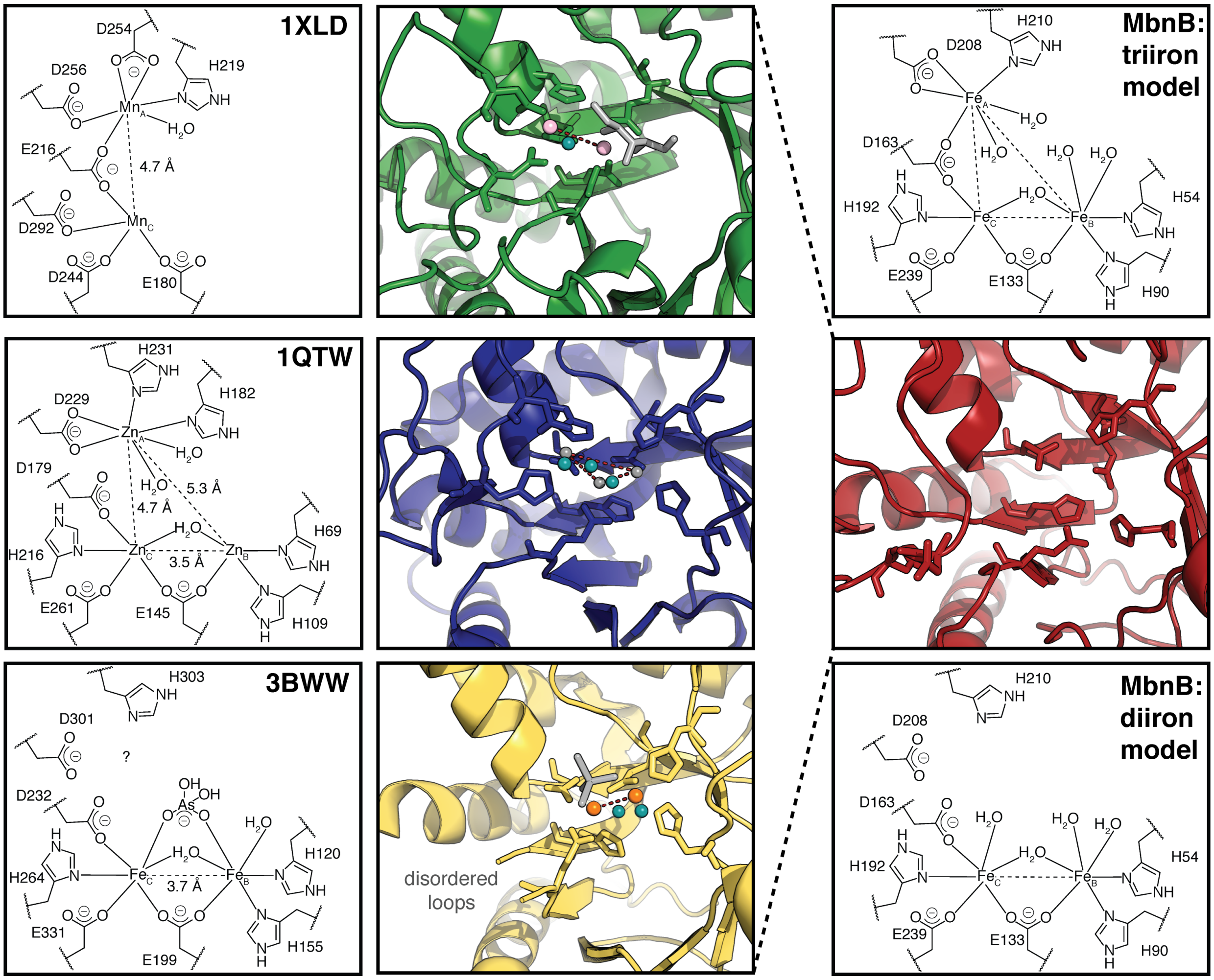

Fig. S21. Comparison of the metal binding sites of xylose isomerase (PDB: 1XLD), endonuclease IV (PDB: 1QTW), *Hs. somnus* 192Pt DUF692 protein (PDB: 3BWW), and possible multinuclear iron sites in MbnB.

For both xylose isomerase and endonuclease IV, the metal-bound crystal structure with the most well-defined active site was structurally aligned against the extant DUF692 structure and the iTasser model of MbnB. The metal sites are labeled A, B, and C to illustrate potential correspondence with the iron sites discussed in the analysis of the MbnB Mössbauer data (Supplemental Text). Xylose isomerase from *Arthrobacter* sp. NRRL B3728 (top left) utilizes a dimanganese site (although some enzymes in this family utilize a dimagnesium site or a single divalent metal). The ligands to the metal site C are present in DUF692 enzymes (including MbnB), and two of the three amino acid ligands for the metal site A are conserved (*63*). Manganese ions are shown in pink, and water molecules are shown in teal. Both metal binding sites A and C are conserved in the *E. coli* endonuclease IV enzyme (center left), and a third metal site (site B) is also present; in these enzymes, all three sites are occupied by zinc (*64*). Zinc ions are show in gray, and water molecules are shown in teal. The sole structurally characterized DUF692 protein (bottom left) has a diiron site, corresponding to metal binding sites C and B in the endonuclease IV family. It is unclear whether metal binding site A is conserved. Two of the amino acid ligands are conserved, but are part of an extended loop that is disordered and not visible in structure. An arsenate group observed in the crystal structure is likely a crystallographic artifact. Iron ions are shown in orange, and water molecules are shown in teal. If *Ms. trichosporium* OB3b MbnB and its homologues form a trinuclear iron site (top right), these two conserved ligands (D208 and H210) may stabilize metal site A, and D163 may bridge the metals in metal sites A and C (as it does in xylose isomerase but not in endonuclease IV). The remaining two iron sites (C and B) are largely homologous to those observed in the DUF692 structure. If MbnB forms a dinuclear iron site (bottom right), D208 and H210 may not be involved in metal coordination, and the resultant diiron active site could fully resemble the site seen in the DUF692 structure.

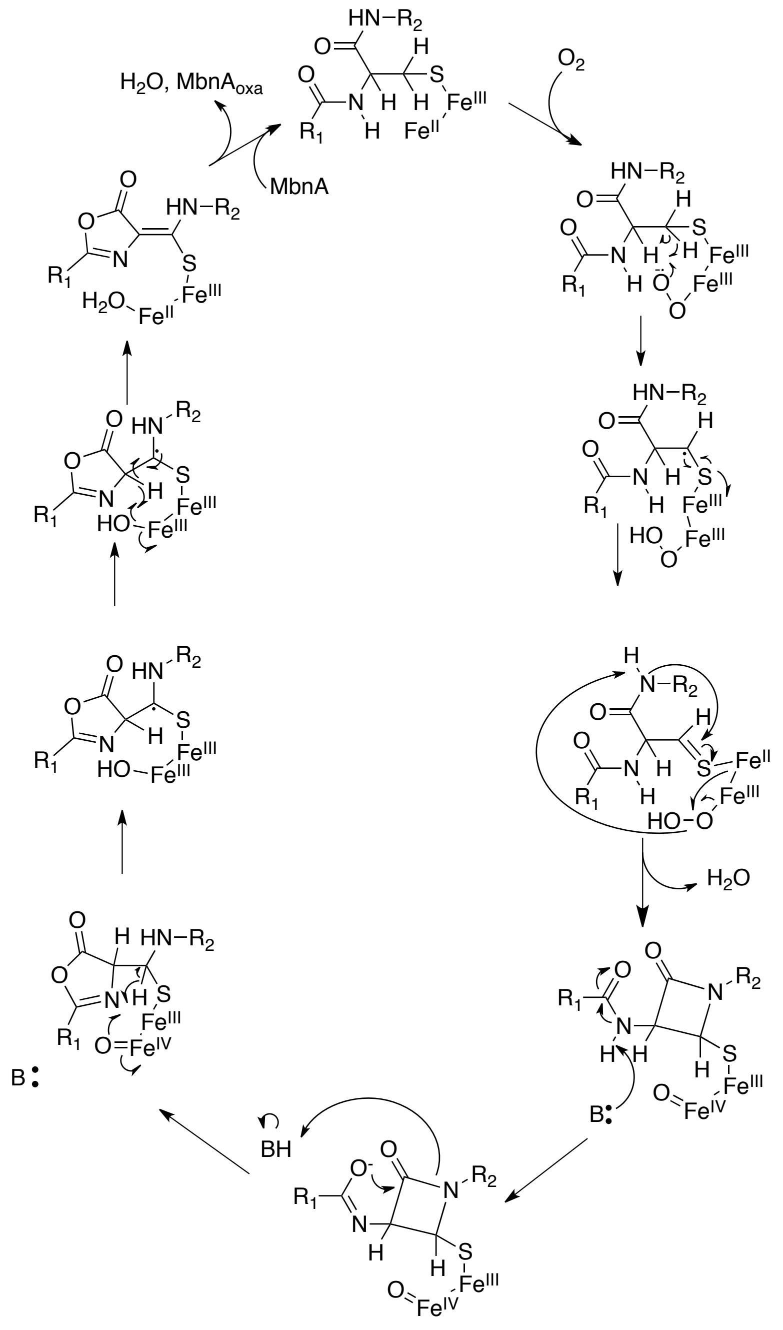

Fig. S22. Possible mechanism for MbnBC-catalyzed generation of oxazolone/thioamide moieties on MbnA.

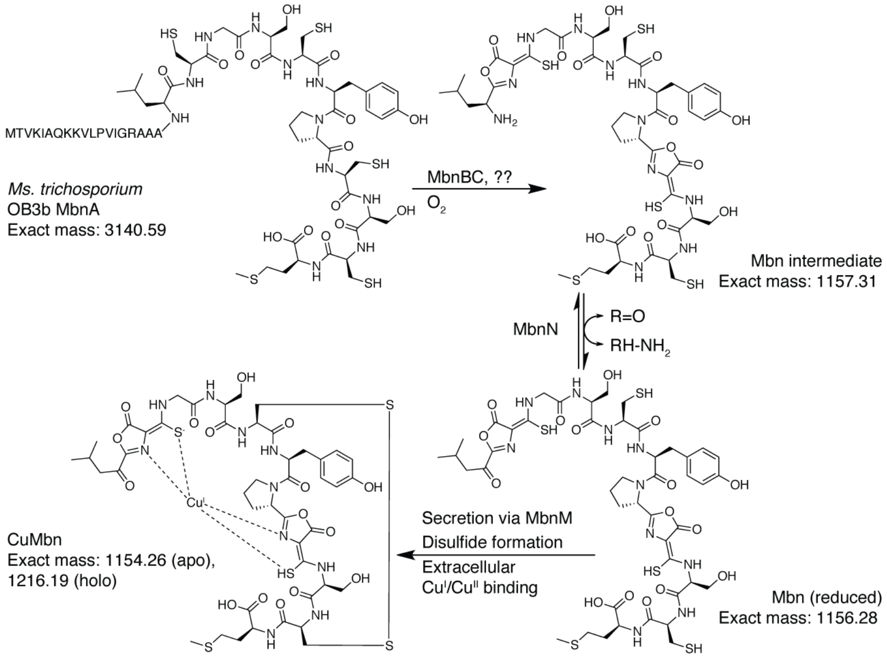

Fig. S23. Mbn biosynthesis from MbnA by MbnBC and MbnN.

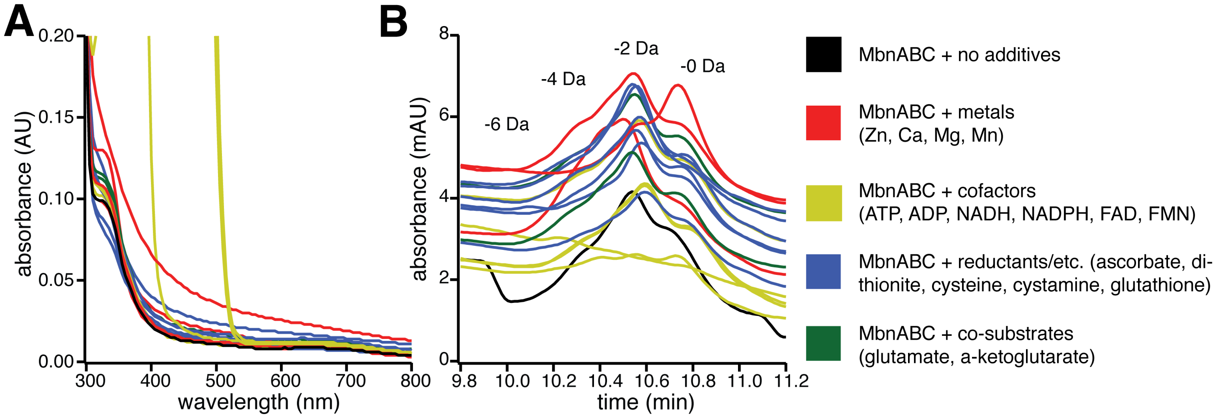

Fig. S24. Addition of a wide range of candidate co-substrates and co-factors does not appear to affect MbnABC reactivity.

(**A**) Overlaid post-activity UV-vis spectra for reactions containing 100 μM anaerobic MbnBC, 125 μM MbnA, and 125 μM additive in aerobically prepared buffer. To investigate the potential catalytic relevance of a highly-conserved lysine in MbnC, identical reactions were carried out with anaerobic enzyme that had been incubated with 500 μM PLP, with excess cofactor removed via a PD-10 column; barring the presence of absorption features associated with PLP binding, results were identical. (**B**) Overlaid UV-LC-MS chromatograms for reactions without PLP, at the elution point of the peptide. Although addition of some cofactors shifted the ratio of the mass species observed (-6 Da, -4 Da, -2 Da, and unmodified), the same masses were observed in all reactions as in the control reaction.

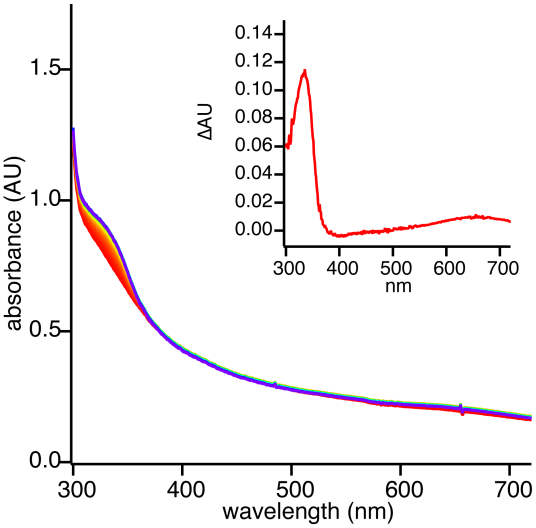

Fig. S25. Addition of small amounts of cell lysate from Mbn-producing *Ms. trichosporium* OB3b cells does not affect MbnABC activity.

UV-vis spectra for MbnABC reactions in the presence of small amounts of lysate taken over 30 min shown formation of the same features observed in the in vitro reaction without the lysate addition (difference spectrum in inset), although the use of UV-vis spectrophotometry to track reactions precluded higher levels of lysate.

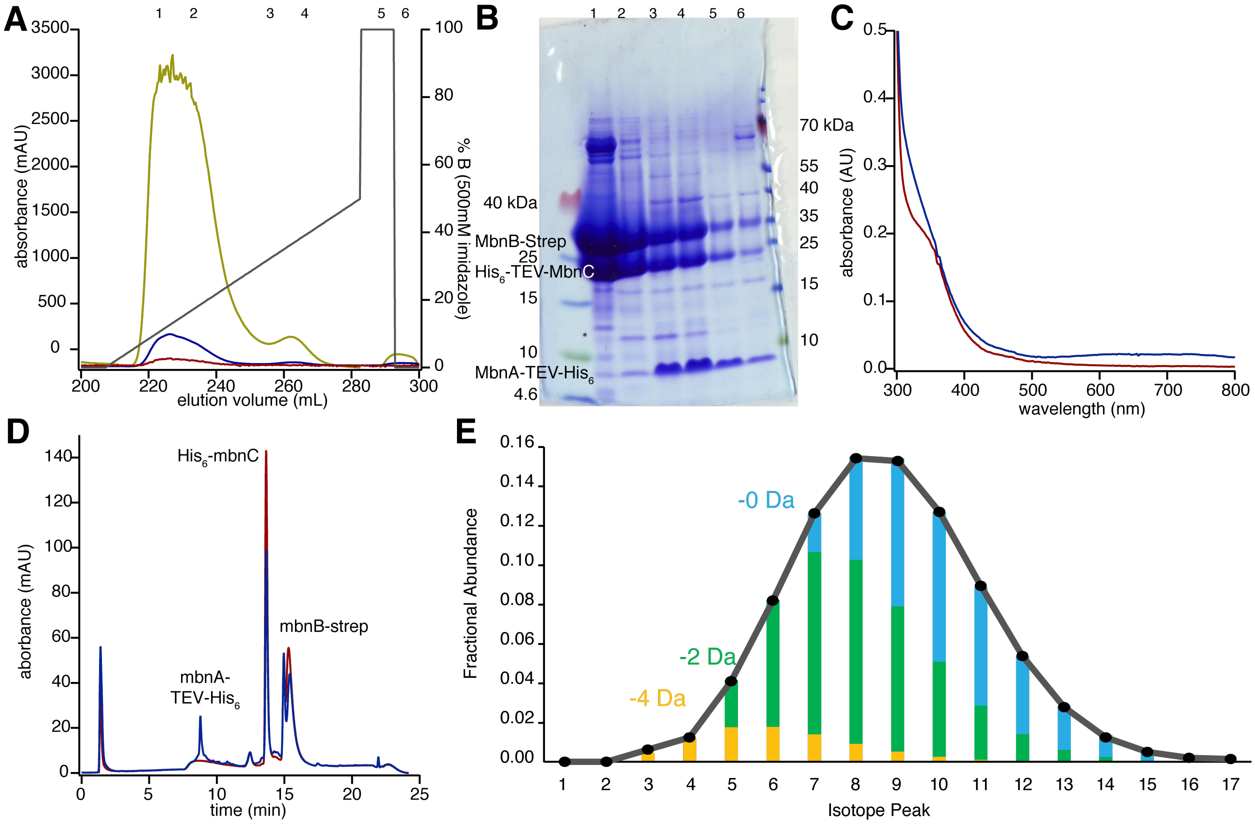

Fig. S26. Heterologous co-expression of MbnBC and C-terminally His$_{10}$-tagged MbnA from *Vi. caribbenthicus* BAA-2122 does not result in leader peptide cleavage.

(**A**) Chromatograms (280 nm in yellow, 330 nm in blue, 400 nm in red) of Ni-affinity elution profile. The first peak consists primarily of the heterodimeric MbnBC complex, with a small amount of peptide and some contaminant proteins from the heterologous expression host, *E. coli*. The smaller, second peak contains a larger amount of the peptide substrate, along with some MbnBC. (**B**) SDS-PAGE of elution fractions numbered in the chromatogram in part (**A**). (**C**) UV-Vis spectra for the first elution peak (red) and the second peak (blue). The protein peak exhibits primarily the feature associated with oxidation of iron in MbnB; the second peak exhibits additional characteristics associated with the modified peptide (the 335 nm feature observed in *Ms. trichosporium* OB3b is slightly UV-shifted in this species) and the peptide protein complex (the broad 650 nm feature). (**D**) LC-UV-MS chromatograms for both peaks. The first peak, in red, has no peptide feature. A peptide elution feature is visible for the second peak, in blue. (**E**) Distribution of masses observed for this peptide. As with in vitro reactions, a mix of unmodified and modified reactions are observed, although the etiology of the -2 Da shift predicted by deconvolution is unclear, since this peptide contains a single cysteine. Regardless no leader peptide cleavage is observed.

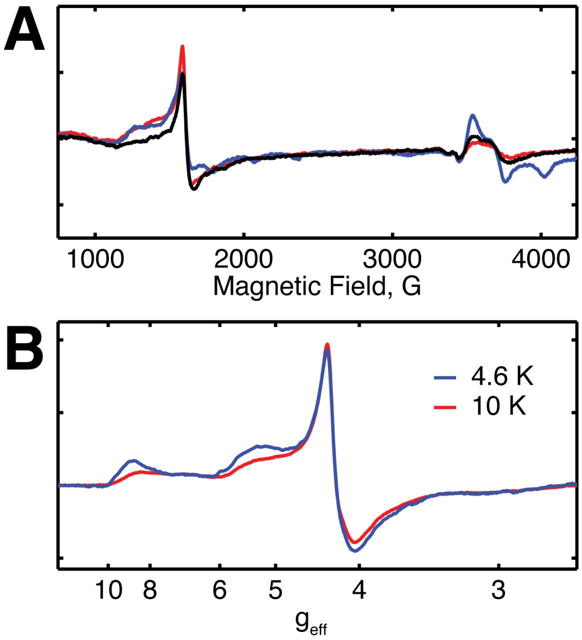

Fig. S27. Electron paramagnetic resonance spectra of MbnBC complexes.

(**A**) Overlay of spectra of aerobically-isolated MbnBC complexes from *Ms. trichosporium* OB3b (blue), *Co. composti* DSM 21721 (red), and *Ps.* sp. ST29 (black), collected at 10 K. (**B**) expanded view of the low-field features of *Ms. trichosporium* OB3b MbnBC, collected at 4.6 K (blue) and 10 K (red). Measurements were performed on a Bruker ESP 300 spectrometer at 4.6 or 10 K with microwave frequencies 9.623 GHz (top) 9.480 GHz (bottom, 10 K), and 9.621 GHz (bottom, 4.6 K), microwave powers 2 mW (top) and 20 mW (bottom), 10 G modulation amplitude, and 80 ms time constant and conversion time.

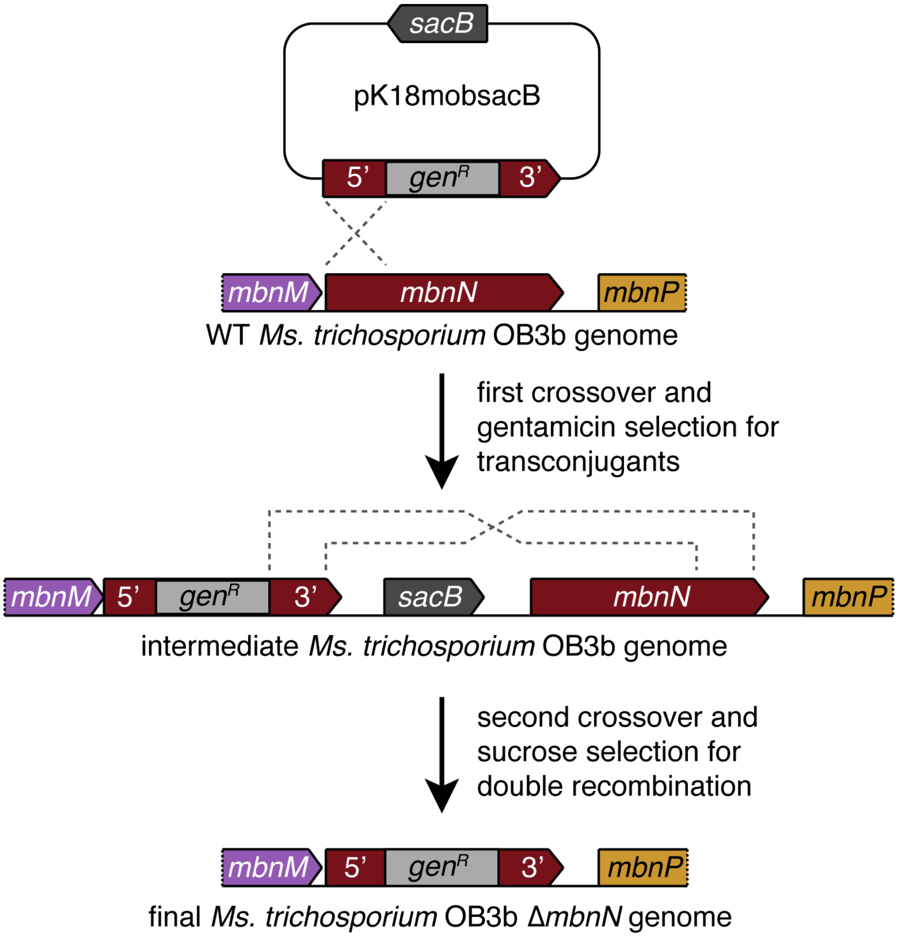

Fig. S28. Cloning scheme for *mbnN* knockout construction in *Ms. trichosporium* OB3b.

Table S1. Metal loading for all species/constructs of MbnBC, as determined by ICP-OES.

Construct	Fe per heterodimer	Ni per heterodimer	Zn per heterodimer
Ms. trichosporium OB3b			
His$_6$-TEV-MbnC, MbnB-Strep	1.325 ± .192	.281 ± .037	.202 ± .139
His$_6$-TEV-MbnC, MbnB$_{H54A}$-Strep	.826 ± .453	1.521 ± 2.113	1.162 ± .866
His$_6$-TEV-MbnC, MbnB$_{H90S}$-Strep	1.311 ± .659	.133 ± .072	.330 ± .213
His$_6$-TEV-MbnC, MbnB$_{E133A}$-Strep	.402 ± .460	.089 ± .051	.193 ± .237
His$_6$-TEV-MbnC, MbnB$_{D163S}$-Strep	.438 ± .166	.262 ± .133	.199 ± .041
His$_6$-TEV-MbnC, MbnB$_{H192A}$-Strep	1.195 ± .618	.176 ± .049	.510 ± ,190
His$_6$-TEV-MbnC, MbnB$_{E239A}$-Strep	.834 ± .510	.111 ± .068	.174 ± .045
His$_6$-TEV-MbnC, MbnB$_{E133A,E239A}$-Strep	.028 ± .005	.610 ± .020	.320 ± .292
Mc. hirsuta CSC1			
His$_6$-TEV-MbnC, MbnB-S•tag	1.492 ± .495	.243 ± .207	.215 ± .086
Co. composti DSM 21721			
His$_6$-TEV-MbnC, MbnB- S•tag	1.958 ± .788	.052 ± .133	.118 ± .139
Ps. sp. ST29			
His$_6$-TEV-MbnC, MbnB-Strep	2.372 ± .459	.014 ± .071	.030 ± .093
Gl. sp. SXCC-1			
His$_6$-TEV-MbnC, MbnB-Strep	1.819 ± .412	.174 ± .116	.284 ± .172
Vi. caribbenthicus BAA-2122			
His$_6$-TEV-MbnC, MbnB-Strep	2.701 ± 1.439	.084 ± .080	.099 ± .095

All values are the mean and standard deviation of the measured metal concentrations for three independent protein preparations.

Table S2. Bacterial strains and plasmids used in this study.

Strains	Genotype/phenotype	Reference /source
Ms. trichosporium		
OB3b	Wild-type OB3b	ATCC
OB3b Δ*mbnN*	OB3b Gen^{R} Δ*mbnN*	This study
E. coli		
Top10	F– *mcrA* Δ(*mrr-hsdRMS-mcrBC*) Φ80*lacZΔM15* Δ*lacX74 recA1 araD139* Δ(*ara leu*) 7697 *galU galK rpsL* (StrR) *endA1 nupG*	Thermo Fisher (Invitrogen)
NiCo21 (DE3)	F– *can::CBD fhuA2 [lon] ompT gal (λ DE3) [dcm] arnA::CBD slyD::CBD glmS6Ala* Δ*hsdS*	New England Biolabs
LOBSTR-RIL (DE3)	F– *arnA*$_{H359S,H361S,H592S,H593S}$ *slyD*$_{1-150}$ *fhuA2 [lon] ompT gal (λ DE3) [dcm]* Δ*hsdS* [*argU ileY leuW* Cam^{R}]	Kerafast
Plasmids		
pACYCDuet-1	Two cloning sites; P15A ori, Cam^{R}	Novagen
pACYCDuet-1::OB3b-HCBS	Gene fragment containing a TEV cleavage site, the codon-optimized *Ms. trichosporium* OB3b *mbnC* gene into CDS-1 of pACYCDuet-1; gene fragment containing the codon-optimized *mbnB* gene from the same operon and a C-terminal Strep tag into CDS-2.	This study
pACYCDuet-1::OB3b-HBCS	Gene fragment containing a TEV cleavage site, the OB3b *mbnB* gene into CDS-1 of pACYCDuet-1; gene fragment containing the OB3b *mbnC* gene and a C-terminal Strep tag into CDS-2.	This study
pACYCDuet-1::OB3b-HBC	Gene fragment containing a TEV cleavage site, the OB3b *mbnB* gene into CDS-1 of pACYCDuet-1; gene fragment containing the OB3b *mbnB* gene and a stop codon into CDS-2.	This study
pACYCDuet-1::OB3b-HCB	Gene fragment containing a TEV cleavage site, the OB3b *mbnC* gene into CDS-1 of pACYCDuet-1; gene fragment containing the OB3b *mbnB* gene and a C-terminal stop codon into CDS-2.	This study
pACYCDuet-1::OB3b-HCB$_{H54A}$S	pACYCDuet-1::OB3b-HCBS with H54A mutation in *mbnB*	This study
pACYCDuet-1::OB3b-HCB$_{H90S}$S	pACYCDuet-1::OB3b-HCBS with H90S mutation in *mbnB*	This study
pACYCDuet-1::OB3b-HCB$_{E133A}$S	pACYCDuet-1::OB3b-HCBS with E133A mutation in *mbnB*	This study
pACYCDuet-1::OB3b-HCB$_{D163S}$S	pACYCDuet-1::OB3b-HCBS with D163S mutation in *mbnB*	This study
pACYCDuet-1::OB3b-HCB$_{H192A}$S	pACYCDuet-1::OB3b-HCBS with H192A mutation in *mbnB*	This study
pACYCDuet-1::OB3b-HCB$_{E239A}$S	pACYCDuet-1::OB3b-HCBS with E239A mutation in *mbnB*	This study
pCDFDuet-1	Two cloning sites; CloDF13 ori, Kan^{R}	Novagen
pCDFDuet-1::CSC1-HCBS	Gene fragment containing a TEV cleavage site, the codon-optimized *Mc. hirsuta* CSC1 *mbnC* gene into CDS-1 of pCDFDuet-1; gene fragment containing the codon-optimized *mbnB* gene from the same species and a C-terminal S•tag into CDS-2.	This study
pCDFDuet-1::LW3II-HCBS	Gene fragment containing a TEV cleavage site, the codon-optimized *Ms.* sp. LW3 Type IIb *mbnC* gene into CDS-1 of pCDFDuet-1; gene fragment containing the codon-optimized *mbnB* gene from the same operon and a C-terminal Strep tag into CDS-2.	This study
pCDFDuet-1::Coma-HCBS	Gene fragment containing a TEV cleavage site, the codon-optimized *Co. composti* DSM21721 *mbnC* gene into CDS-1 of pCDFDuet-1 after the N-terminal His$_{6}$ tag; gene fragment containing the codon-optimized *mbnB* gene from the same species and a C-terminal S•tag into CDS-2.	This study
pCDFDuet-1::ST29-HCBS	Gene fragment containing a TEV cleavage site, the codon-optimized *Ps.* sp. ST29 *mbnC* gene into CDS-1 of pCDFDuet-1; gene fragment containing the codon-optimized *mbnB* gene from the same operon and a C-terminal Strep tag into CDS-2.	This study
pCDFDuet-1::SXCC1-HCBS	Gene fragment containing a TEV cleavage site, the codon-optimized *Gl.* sp. SXCC-1 *mbnC* gene into CDS-1 of pCDFDuet-1; gene fragment containing the codon-optimized *mbnB* gene from the same operon and a C-terminal Strep tag into CDS-2.	This study
pCDFDuet-1::BAA-HCBS	Gene fragment containing a TEV cleavage site, the codon-optimized *Vi. caribbenthicus* BAA-2122 *mbnC* gene into CDS-1 of pCDFDuet-1; gene fragment containing the codon-optimized *mbnB* gene from the same operon and a C-terminal Strep tag into CDS-2.	This study
pCDFDuet-1::ISP5550-HCBS	Gene fragment containing a TEV cleavage site, the codon-optimized *St. katrae* NRRL ISP-5550 *mbnC* gene into CDS-1 of pCDFDuet-1; gene fragment containing the codon-optimized *mbnB* gene from the same operon and a C-terminal Strep tag into CDS-2.	This study
pSGC-His	N-terminal TEV-cleavable His$_{6}$ tag, ColE1 ori, Kan^{R}	Structural

		Genomics Consortium
pSGC-His::OB3b-MbnA	Gene fragment *Ms. trichosporium* OB3b *MbnA* containing an N-terminal TEV-cleavable His$_{6,}$ tag, ColE1 ori, Kan^R	This study
pSGC-His::BAA-MbnA	Gene fragment *Vi. caribbenthicus* BAA-2122 *MbnA* containing an N-terminal TEV-cleavable His$_6$ tag, ColE1 ori, Kan^R	This study
pNYCOMPS	C-terminal TEV-cleavable His$_{10}$ tag, ColE1 ori, Kan^R	New York Constortium on Membrane Protein Structure
pNYCOMPS::OB3b-MbnA	Gene fragment *Ms. trichosporium* OB3b *MbnA* containing a C-terminal TEV-cleavable His$_{10}$ tag, ColE1 ori, Kan^R	This study
pNYCOMPS::BAA-MbnA	Gene fragment *Vi. caribbenthicus* BAA-2122 *MbnA* containing a C-terminal TEV-cleavable His$_{10}$ tag, ColE1 ori, Kan^R	This study

Table S3. List of primers used in this study.

	Forward primer	Reverse primer
Construction of *mbnA* expression vectors		
pSGC-His::OB3b-mbnA	TACTTCCAATCCATGACTGTCAAGATTGCTCAGAAGAAAGTC	TATCCACCTTTACTGTTACATGCAGCTGCACGGATAGC
pSGC-His::BAA-2122-MbnA	TACTTCCAATCCATGAAAAATGATAAGAAAGTAGTTGTAAAAGTGAAAGATAAAG	TATCCACCTTTACTGTTACTTGTTAAAAGCACCGCAAGTCATTTC
pNYCOMPS::OB3b-MbnA	TTAAGAAGGAGATATACTATGACTGTCAAGATTGCTCAGAAGAAAGTC	TGAAAATAGAGGTTTTCGGCCATGCAGCTGCACGGATAGC
pNYCOMPS::BAA-2122-MbnA	TTAAGAAGGAGATATACTATGAAAAATGATAAGAAAGTAGTTGTAAAAGTGAAAGATAAAG	TGAAAATAGAGGTTTTCGGCCTTGTTAAAAGCACCGCAAGTCATTTC
Mutagenesis of *mbnB*		
pACYCDuet-1::OB3b-HCB$_{H54A}$S	ATATTTAGACAGCATAATGGCGAAGGCCACCGGGCAGTC	GACTGCCCGGTGGCCTTCGCCATTATGCTGTCTAAATAT
pACYCDuet-1::OB3b-HCB$_{H90S}$S	TATGCGTAAAGTACAGGAGATGGTCACTAACGTACACCGGG	CCCGGTGTACGTTAGTGACCATCTCCTGTACTTTACGCATA
pACYCDuet-1::OB3b-HCB$_{E133A}$S	ATAATAGACGGATAGTTTGCCAGATACAGACGGGTGC	GCACCCGTCTGTATCTGGCAAACTATCCGTCTATTAT
pACYCDuet-1::OB3b-HCB$_{D163S}$S	CAAATGGCGTTAGACGCAGAGAACAGAACACCCACGCC	GGCGTGGGTGTTCTGTTCTCTGCGTCTAACGCCATTTG
pACYCDuet-1::OB3b-HCB$_{H192A}$S	GTAGCCAGCGACGGCAAAATGACGCGTGGTTTCGATAATC	GATTATCGAAACCACGCGTCATTTTGCCGTCGCTGGCTAC
pACYCDuet-1::OB3b-HCB$_{E239A}$S	ATCAATGTCAAAATCACGTGCATAGGTAATGGTGGCACC	GGTGCCACCATTACCTATGCACGTGATTTTGACATTGAT
Δ*mbnN* construction		
mbnN 5’ region	AAACAGCTATGACATGATTAATGACGGCGATCCCATGTGAAA	AGTCGAGGCATTTCTGTCCTCGTCTCTCGCTCTATGGAAAGCC
Gentamicin resistance gene	AGGACAGAAATGCCTCGACTTCG	TTAGGTGGCGGTACTTGGGTCG
mbnN 3’ region	ACCCAAGTACCGCCACCTAATTCGACGCTCTCGCTTCCGAT	TCCCAGTCACGACGTTGTAACGTGGATCGTCGATTCCTGTCTC
pk18mobsacB vector	TTACAACGTCGTGACTGGGAAA	TAATCATGTCATAGCTGTTTCCTGTGT

Additional Data File S1. Amino acid sequences for MbnB homologues.
Original multifasta file of DUF692 sequences derived from the JGI/IMG and NCBI databases and used to construct the DUF692 sequence similarity network.

Additional Data File S2. MbnB homologue metadata.
Metadata related to DUF692 sequences.

Additional Data File S3. MbnB homologue sequence similarity network.
Cytoscape-formatted sequence similarity network for DUF692 sequences.

Additional Data File S4. Amino acid sequences for MbnC homologues.
Original multifasta file of TIGR04160 and TIGR04061 sequences derived from the JGI/IMG and NCBI databases and used to construct the MbnC homologue sequence similarity network.

Additional Data File S5. MbnC homologue metadata.
Metadata related to TIGR04160 and TIGR04061 sequences.

Additional Data File S6. MbnC homologue sequence similarity network.
Cytoscape-formatted sequence similarity network for MbnC homologue sequences.

Additional Data File S7. MultiGenBank file of MbnBC constructs.
Contains Duet vector constructs for all MbnB/MbnC co-expression systems used in this work.

References

1. A. Butler, Acquisition and utilization of transition metal ions by marine organisms. *Science* **281**, 207–210 (1998). doi:10.1126/science.281.5374.207 Medline

2. L. D. Palmer, E. P. Skaar, Transition metals and virulence in bacteria. *Annu. Rev. Genet.* **50**, 67–91 (2016). doi:10.1146/annurev-genet-120215-035146 Medline

3. M. Nairz, A. Schroll, T. Sonnweber, G. Weiss, The struggle for iron—a metal at the host-pathogen interface. *Cell. Microbiol.* **12**, 1691–1702 (2010). doi:10.1111/j.1462-5822.2010.01529.x Medline

4. M. Miethke, M. A. Marahiel, Siderophore-based iron acquisition and pathogen control. *Microbiol. Mol. Biol. Rev.* **71**, 413–451 (2007). doi:10.1128/MMBR.00012-07 Medline

5. G. Ghssein, C. Brutesco, L. Ouerdane, C. Fojcik, A. Izaute, S. Wang, C. Hajjar, R. Lobinski, D. Lemaire, P. Richaud, R. Voulhoux, A. Espaillat, F. Cava, D. Pignol, E. Borezée-Durant, P. Arnoux, Biosynthesis of a broad-spectrum nicotianamine-like metallophore in *Staphylococcus aureus*. *Science* **352**, 1105–1109 (2016). doi:10.1126/science.aaf1018 Medline

6. P. T. Chivers, E. L. Benanti, V. Heil-Chapdelaine, J. S. Iwig, J. L. Rowe, Identification of Ni-(L-His)$_2$ as a substrate for NikABCDE-dependent nickel uptake in *Escherichia coli*. *Metallomics* **4**, 1043–1050 (2012). doi:10.1039/c2mt20139a Medline

7. M. V. Cherrier, C. Cavazza, C. Bochot, D. Lemaire, J. C. Fontecilla-Camps, Structural characterization of a putative endogenous metal chelator in the periplasmic nickel transporter NikA. *Biochemistry* **47**, 9937–9943 (2008). doi:10.1021/bi801051y Medline

8. K. S. Chaturvedi, C. S. Hung, J. R. Crowley, A. E. Stapleton, J. P. Henderson, The siderophore yersiniabactin binds copper to protect pathogens during infection. *Nat. Chem. Biol.* **8**, 731–736 (2012). doi:10.1038/nchembio.1020 Medline

9. C. W. Johnston, M. A. Wyatt, X. Li, A. Ibrahim, J. Shuster, G. Southam, N. A. Magarvey, Gold biomineralization by a metallophore from a gold-associated microbe. *Nat. Chem. Biol.* **9**, 241–243 (2013). doi:10.1038/nchembio.1179 Medline

10. T. C. Johnstone, E. M. Nolan, Beyond iron: Non-classical biological functions of bacterial siderophores. *Dalton Trans.* **44**, 6320–6339 (2015). doi:10.1039/C4DT03559C Medline

11. L. M. K. Dassama, G. E. Kenney, A. C. Rosenzweig, Methanobactins: From genome to function. *Metallomics* **9**, 7–20 (2017). doi:10.1039/C6MT00208K Medline

12. H. J. Kim, D. W. Graham, A. A. DiSpirito, M. A. Alterman, N. Galeva, C. K. Larive, D. Asunskis, P. M. Sherwood, Methanobactin, a copper-acquisition compound from methane-oxidizing bacteria. *Science* **305**, 1612–1615 (2004). doi:10.1126/science.1098322 Medline

13. B. D. Krentz, H. J. Mulheron, J. D. Semrau, A. A. Dispirito, N. L. Bandow, D. H. Haft, S. Vuilleumier, J. C. Murrell, M. T. McEllistrem, S. C. Hartsel, W. H. Gallagher, A comparison of methanobactins from *Methylosinus trichosporium* OB3b and *Methylocystis* strain Sb2 predicts methanobactins are synthesized from diverse peptide precursors modified to create a common core for binding and reducing copper ions. *Biochemistry* **49**, 10117–10130 (2010). doi:10.1021/bi1014375 Medline

14. G. E. Kenney, M. Sadek, A. C. Rosenzweig, Copper-responsive gene expression in the methanotroph *Methylosinus trichosporium* OB3b. *Metallomics* **8**, 931–940 (2016). doi:10.1039/C5MT00289C Medline

15. G. E. Kenney, A. C. Rosenzweig, Genome mining for methanobactins. *BMC Biol.* **11**, 17 (2013). doi:10.1186/1741-7007-11-17 Medline

16. J. D. Semrau, S. Jagadevan, A. A. DiSpirito, A. Khalifa, J. Scanlan, B. H. Bergman, B. C. Freemeier, B. S. Baral, N. L. Bandow, A. Vorobev, D. H. Haft, S. Vuilleumier, J. C. Murrell, Methanobactin and MmoD work in concert to act as the 'copper-switch' in methanotrophs. *Environ. Microbiol.* **15**, 3077–3086 (2013). Medline

17. P. G. Arnison, M. J. Bibb, G. Bierbaum, A. A. Bowers, T. S. Bugni, G. Bulaj, J. A. Camarero, D. J. Campopiano, G. L. Challis, J. Clardy, P. D. Cotter, D. J. Craik, M. Dawson, E. Dittmann, S. Donadio, P. C. Dorrestein, K.-D. Entian, M. A. Fischbach, J. S. Garavelli, U. Göransson, C. W. Gruber, D. H. Haft, T. K. Hemscheidt, C. Hertweck, C. Hill, A. R. Horswill, M. Jaspars, W. L. Kelly, J. P. Klinman, O. P. Kuipers, A. J. Link, W. Liu, M. A. Marahiel, D. A. Mitchell, G. N. Moll, B. S. Moore, R. Müller, S. K. Nair, I. F. Nes, G. E. Norris, B. M. Olivera, H. Onaka, M. L. Patchett, J. Piel, M. J. T. Reaney, S. Rebuffat, R. P. Ross, H.-G. Sahl, E. W. Schmidt, M. E. Selsted, K. Severinov, B. Shen, K. Sivonen, L. Smith, T. Stein, R. D. Süssmuth, J. R. Tagg, G.-L. Tang, A. W. Truman, J. C. Vederas, C. T. Walsh, J. D. Walton, S. C. Wenzel, J. M. Willey, W. A. van der Donk, Ribosomally synthesized and post-translationally modified peptide natural products: Overview and recommendations for a universal nomenclature. *Nat. Prod. Rep.* **30**, 108–160 (2013). doi:10.1039/C2NP20085F Medline

18. U. Rix, J. Zheng, L. L. Remsing Rix, L. Greenwell, K. Yang, J. Rohr, The dynamic structure of jadomycin B and the amino acid incorporation step of its biosynthesis. *J. Am. Chem. Soc.* **126**, 4496–4497 (2004). doi:10.1021/ja031724o Medline

19. S. Behnken, C. Hertweck, Anaerobic bacteria as producers of antibiotics. *Appl. Microbiol. Biotechnol.* **96**, 61–67 (2012). doi:10.1007/s00253-012-4285-8 Medline

20. M. Izawa, T. Kawasaki, Y. Hayakawa, Cloning and heterologous expression of the thioviridamide biosynthesis gene cluster from *Streptomyces olivoviridis*. *Appl. Environ. Microbiol.* **79**, 7110–7113 (2013). doi:10.1128/AEM.01978-13 Medline

21. D. D. Nayak, N. Mahanta, D. A. Mitchell, W. W. Metcalf, Post-translational thioamidation of methyl-coenzyme M reductase, a key enzyme in methanogenic and methanotrophic Archaea. *eLife* **6**, e29218 (2017). doi:10.7554/eLife.29218 Medline

22. L. A. Behling, S. C. Hartsel, D. E. Lewis, A. A. DiSpirito, D. W. Choi, L. R. Masterson, G. Veglia, W. H. Gallagher, NMR, mass spectrometry and chemical evidence reveal a different chemical structure for methanobactin that contains oxazolone rings. *J. Am. Chem. Soc.* **130**, 12604–12605 (2008). doi:10.1021/ja804747d Medline

23. A. El Ghazouani, A. Baslé, J. Gray, D. W. Graham, S. J. Firbank, C. Dennison, Variations in methanobactin structure influences copper utilization by methane-oxidizing bacteria. *Proc. Natl. Acad. Sci. U.S.A.* **109**, 8400–8404 (2012). doi:10.1073/pnas.1112921109 Medline

24. G. E. Kenney, A. W. Goering, M. O. Ross, C. J. DeHart, P. M. Thomas, B. M. Hoffman, N. L. Kelleher, A. C. Rosenzweig, Characterization of methanobactin from *Methylosinus* sp. LW4. *J. Am. Chem. Soc.* **138**, 11124–11127 (2016). doi:10.1021/jacs.6b06821 Medline

25. N. Nagano, C. A. Orengo, J. M. Thornton, One fold with many functions: The evolutionary relationships between TIM barrel families based on their sequences, structures and functions. *J. Mol. Biol.* **321**, 741–765 (2002). doi:10.1016/S0022-2836(02)00649-6 Medline

26. B. J. Burkhart, G. A. Hudson, K. L. Dunbar, D. A. Mitchell, A prevalent peptide-binding domain guides ribosomal natural product biosynthesis. *Nat. Chem. Biol.* **11**, 564–570 (2015). doi:10.1038/nchembio.1856 Medline

27. N. H. Tolia, L. Joshua-Tor, Strategies for protein coexpression in *Escherichia coli*. *Nat. Methods* **3**, 55–64 (2006). doi:10.1038/nmeth0106-55 Medline

28. B. J. Wallar, J. D. Lipscomb, Dioxygen activation by enzymes containing binuclear non-heme iron clusters. *Chem. Rev.* **96**, 2625–2658 (1996). doi:10.1021/cr9500489 Medline

29. M. Costas, M. P. Mehn, M. P. Jensen, L. Que Jr., Dioxygen activation at mononuclear nonheme iron active sites: Enzymes, models, and intermediates. *Chem. Rev.* **104**, 939–986 (2004). doi:10.1021/cr020628n Medline

30. C. A. Brown, G. J. Remar, R. L. Musselman, E. I. Solomon, Spectroscopic and electronic structure studies of met-hemerythrin model complexes: A description of the ferric-oxo dimer bond. *Inorg. Chem.* **34**, 688–717 (1995). doi:10.1021/ic00107a024

31. H. J. Kim, N. Galeva, C. K. Larive, M. Alterman, D. W. Graham, Purification and physical-chemical properties of methanobactin: A chalkophore from *Methylosinus trichosporium* OB3b. *Biochemistry* **44**, 5140–5148 (2005). doi:10.1021/bi047367r Medline

32. E. Tamanaha, B. Zhang, Y. Guo, W. C. Chang, E. W. Barr, G. Xing, J. St Clair, S. Ye, F. Neese, J. M. Bollinger Jr., C. Krebs, Spectroscopic evidence for the two C–H-cleaving

intermediates of *Aspergillus nidulans* isopenicillin N synthase. *J. Am. Chem. Soc.* **138**, 8862–8874 (2016). doi:10.1021/jacs.6b04065 Medline

33. S. C. Peck, C. Wang, L. M. K. Dassama, B. Zhang, Y. Guo, L. J. Rajakovich, J. M. Bollinger Jr., C. Krebs, W. A. van der Donk, O–H activation by an unexpected ferryl intermediate during catalysis by 2-hydroxyethylphosphonate dioxygenase. *J. Am. Chem. Soc.* **139**, 2045–2052 (2017). doi:10.1021/jacs.6b12147 Medline

34. G. Xing, Y. Diao, L. M. Hoffart, E. W. Barr, K. S. Prabhu, R. J. Arner, C. C. Reddy, C. Krebs, J. M. Bollinger Jr., Evidence for C-H cleavage by an iron-superoxide complex in the glycol cleavage reaction catalyzed by myo-inositol oxygenase. *Proc. Natl. Acad. Sci. U.S.A.* **103**, 6130–6135 (2006). doi:10.1073/pnas.0508473103 Medline

35. B. Wörsdörfer, M. Lingaraju, N. H. Yennawar, A. K. Boal, C. Krebs, J. M. Bollinger Jr., M.-E. Pandelia, Organophosphonate-degrading PhnZ reveals an emerging family of HD domain mixed-valent diiron oxygenases. *Proc. Natl. Acad. Sci. U.S.A.* **110**, 18874–18879 (2013). doi:10.1073/pnas.1315927110 Medline

36. A. Trehoux, J.-P. Mahy, F. Avenier, A growing family of O_2 activating dinuclear iron enzymes with key catalytic diiron(III)-peroxo intermediates: Biological systems and chemical models. *Coord. Chem. Rev.* **322**, 142–158 (2016). doi:10.1016/j.ccr.2016.05.014

37. D. Sardar, Z. Lin, E. W. Schmidt, Modularity of RiPP enzymes enables designed synthesis of decorated peptides. *Chem. Biol.* **22**, 907–916 (2015). doi:10.1016/j.chembiol.2015.06.014 Medline

38. A. J. van Heel, D. Mu, M. Montalbán-López, D. Hendriks, O. P. Kuipers, Designing and producing modified, new-to-nature peptides with antimicrobial activity by use of a combination of various lantibiotic modification enzymes. *ACS Synth. Biol.* **2**, 397–404 (2013). doi:10.1021/sb3001084 Medline

39. A. Ala, A. P. Walker, K. Ashkan, J. S. Dooley, M. L. Schilsky, Wilson’s disease. *Lancet* **369**, 397–408 (2007). doi:10.1016/S0140-6736(07)60196-2 Medline

40. K. H. Summer, J. Lichtmannegger, N. Bandow, D. W. Choi, A. A. DiSpirito, B. Michalke, The biogenic methanobactin is an effective chelator for copper in a rat model for Wilson disease. *J. Trace Elem. Med. Biol.* **25**, 36–41 (2011). doi:10.1016/j.jtemb.2010.12.002 Medline

41. J. Lichtmannegger, C. Leitzinger, R. Wimmer, S. Schmitt, S. Schulz, Y. Kabiri, C. Eberhagen, T. Rieder, D. Janik, F. Neff, B. K. Straub, P. Schirmacher, A. A. DiSpirito, N. Bandow, B. S. Baral, A. Flatley, E. Kremmer, G. Denk, F. P. Reiter, S. Hohenester, F. Eckardt-Schupp, N. A. Dencher, J. Adamski, V. Sauer, C. Niemietz, H. H. J. Schmidt, U. Merle, D. N. Gotthardt, G. Kroemer, K. H. Weiss, H. Zischka, Methanobactin reverses

acute liver failure in a rat model of Wilson disease. *J. Clin. Invest.* **126**, 2721–2735 (2016). doi:10.1172/JCI85226 Medline

42. K. Katoh, D. M. Standley, MAFFT: Iterative refinement and additional methods. *Methods Mol. Biol.* **1079**, 131–146 (2014). doi:10.1007/978-1-62703-646-7_8 Medline

43. A. M. Waterhouse, J. B. Procter, D. M. A. Martin, M. Clamp, G. J. Barton, Jalview Version 2—a multiple sequence alignment editor and analysis workbench. *Bioinformatics* **25**, 1189–1191 (2009). doi:10.1093/bioinformatics/btp033 Medline

44. P. V. Troshin, J. B. Procter, G. J. Barton, Java bioinformatics analysis web services for multiple sequence alignment—JABAWS:MSA. *Bioinformatics* **27**, 2001–2002 (2011). doi:10.1093/bioinformatics/btr304 Medline

45. J. A. Gerlt, J. T. Bouvier, D. B. Davidson, H. J. Imker, B. Sadkhin, D. R. Slater, K. L. Whalen, Enzyme Function Initiative-Enzyme Similarity Tool (EFI-EST): A web tool for generating protein sequence similarity networks. *Biochim. Biophys. Acta* **1854**, 1019–1037 (2015). doi:10.1016/j.bbapap.2015.04.015 Medline

46. L. M. K. Dassama, G. E. Kenney, S. Y. Ro, E. L. Zielazinski, A. C. Rosenzweig, Methanobactin transport machinery. *Proc. Natl. Acad. Sci. U.S.A.* **113**, 13027–13032 (2016). doi:10.1073/pnas.1603578113 Medline

47. P. Shannon, A. Markiel, O. Ozier, N. S. Baliga, J. T. Wang, D. Ramage, N. Amin, B. Schwikowski, T. Ideker, Cytoscape: A software environment for integrated models of biomolecular interaction networks. *Genome Res.* **13**, 2498–2504 (2003). doi:10.1101/gr.1239303 Medline

48. F. W. Studier, Stable expression clones and auto-induction for protein production in E. coli. *Methods Mol. Biol.* **1091**, 17–32 (2014). doi:10.1007/978-1-62703-691-7_2 Medline

49. E. Münck, in *Physical Methods in Bioinorganic Chemistry*, L. Que Jr., Ed. (University Science, Sausalito, CA, ed. 1, 2000), pp. 287–319.

50. M. E. Belov, E. Damoc, E. Denisov, P. D. Compton, S. Horning, A. A. Makarov, N. L. Kelleher, From protein complexes to subunit backbone fragments: A multi-stage approach to native mass spectrometry. *Anal. Chem.* **85**, 11163–11173 (2013). doi:10.1021/ac4029328 Medline

51. O. S. Skinner, P. C. Havugimana, N. A. Haverland, L. Fornelli, B. P. Early, J. B. Greer, R. T. Fellers, K. R. Durbin, L. H. F. Do Vale, R. D. Melani, H. S. Seckler, M. T. Nelp, M. E. Belov, S. R. Horning, A. A. Makarov, R. D. LeDuc, V. Bandarian, P. D. Compton, N. L. Kelleher, An informatic framework for decoding protein complexes by top-down mass spectrometry. *Nat. Methods* **13**, 237–240 (2016). doi:10.1038/nmeth.3731 Medline

52. O. S. Skinner, N. A. Haverland, L. Fornelli, R. D. Melani, L. H. F. Do Vale, H. S. Seckler, P. F. Doubleday, L. F. Schachner, K. Srzentić, N. L. Kelleher, P. D. Compton, Top-down

characterization of endogenous protein complexes with native proteomics. *Nat. Chem. Biol.* **14**, 36–41 (2018). doi:10.1038/nchembio.2515 Medline

53. R. T. Fellers, J. B. Greer, B. P. Early, X. Yu, R. D. LeDuc, N. L. Kelleher, P. M. Thomas, ProSight Lite: Graphical software to analyze top-down mass spectrometry data. *Proteomics* **15**, 1235–1238 (2015). doi:10.1002/pmic.201400313 Medline

54. R. Balasubramanian, G. E. Kenney, A. C. Rosenzweig, Dual pathways for copper uptake by methanotrophic bacteria. *J. Biol. Chem.* **286**, 37313–37319 (2011). doi:10.1074/jbc.M111.284984 Medline

55. A. W. Puri, S. Owen, F. Chu, T. Chavkin, D. A. C. Beck, M. G. Kalyuzhnaya, M. E. Lidstrom, Genetic tools for the industrially promising methanotroph *Methylomicrobium buryatense*. *Appl. Environ. Microbiol.* **81**, 1775–1781 (2015). doi:10.1128/AEM.03795-14 Medline

56. J. W. Peters, G. J. Schut, E. S. Boyd, D. W. Mulder, E. M. Shepard, J. B. Broderick, P. W. King, M. W. W. Adams, [FeFe]- and [NiFe]-hydrogenase diversity, mechanism, and maturation. *Biochim. Biophys. Acta* **1853**, 1350–1369 (2015). doi:10.1016/j.bbamcr.2014.11.021 Medline

57. S. Drüeke, K. Wieghardt, B. Nuber, J. Weiss, E. L. Bominaar, A. Sawaryn, H. Winkler, A. X. Trautwein, A new tetranuclear oxohydroxoiron (III) cluster: Crystal structure, magnetic properties, and EXAFS investigation of $[L_4Fe_4(\mu\text{-}O)_2(\mu\text{-}OH)_4]I_4{\cdot}3H_2O$ (L = 1,4,7-triazacyclononane). *Inorg. Chem.* **28**, 4477–4483 (1989). doi:10.1021/ic00324a011

58. P. Chaudhuri, M. Winter, P. Fleischhauer, W. Haase, U. Flörke, H.-J. Haupt, Synthesis, structure and magnetism of a tetranuclear Fe(III) complex containing an $[Fe_4(\mu_3\text{-}O)_2]^{8+}$ core. *Inorg. Chim. Acta* **212**, 241–249 (1993). doi:10.1016/S0020-1693(00)92331-4

59. W. H. Armstrong, M. E. Roth, S. J. Lippard, Tetranuclear iron-oxo complexes. Synthesis, structure, and properties of species containing the nonplanar $\{Fe_4O_2\}^{8+}$ core and seven bridging carboxylate ligands. *J. Am. Chem. Soc.* **109**, 6318–6326 (1987). doi:10.1021/ja00255a015

60. C. Krebs, J. C. Price, J. Baldwin, L. Saleh, M. T. Green, J. M. Bollinger Jr., Rapid freeze-quench ^{57}Fe Mössbauer spectroscopy: Monitoring changes of an iron-containing active site during a biochemical reaction. *Inorg. Chem.* **44**, 742–757 (2005). doi:10.1021/ic048523l Medline

61. A. Bencini, D. Gatteschi, *Electron Paramagnetic Resonance of Exchange Coupled Systems* (Springer-Verlag, ed. 1, 1990).

62. W. Gu, B. S. Baral, A. A. DiSpirito, J. D. Semrau, An aminotransferase is responsible for the deamination of the N-terminal leucine and required for formation of oxazolone ring A in methanobactin of *Methylosinus trichosporium* OB3b. *Appl. Environ. Microbiol.* **83**, e02619-16 (2016). Medline

63. C. A. Collyer, K. Henrick, D. M. Blow, Mechanism for aldose-ketose interconversion by D-xylose isomerase involving ring opening followed by a 1,2-hydride shift. *J. Mol. Biol.* **212**, 211–235 (1990). doi:10.1016/0022-2836(90)90316-E Medline

64. D. J. Hosfield, Y. Guan, B. J. Haas, R. P. Cunningham, J. A. Tainer, Structure of the DNA repair enzyme endonuclease IV and its DNA complex: Double-nucleotide flipping at abasic sites and three-metal-ion catalysis. *Cell* **98**, 397–408 (1999). doi:10.1016/S0092-8674(00)81968-6 Medline